MASTERARBEIT | MASTER'S THESIS

Titel | Title

Transport Modelling of Greenhouse Gases in Alpine Terrain

verfasst von | submitted by

Johannes Gerwinat BSc

angestrebter akademischer Grad | in partial fulfilment of the requirements for the degree of

Master of Science (MSc)

Wien | Vienna, 2025

Studienkennzahl lt. Studienblatt | Degree programme code as it appears on the student record sheet:	UA 066 614
Studienrichtung lt. Studienblatt | Degree programme as it appears on the student record sheet:	Masterstudium Meteorology and Climate Science
Betreut von | Supervisor:	Univ.-Prof. Mag. Dr. Andreas Stohl

Acknowledgements

I want to express my gratitude to Prof. Andreas Stohl and Dr. Seyed Omid Nabavi, MA, for their guidance and supervision throughout this project, and their patience for my questions and life circumstances. Also, I want to acknowledge Dr. Nabavi's generous efforts that were put into generating the WRF simulations, as well as Dott. Dott. ric. Stefano Serafin for providing his knowledge and expertise to assist with this. Furthermore, I am grateful to Mag. Michael Blaschek, PhD, for technical support; specifically the acquiring of GeoSphere TAWES station observation data. I wish to acknowledge the generous assistance of Dipl.-Ing. Sophie Wittig and Anjumol Raju, M.Sc. PhD, by providing me with FLEXPART-ECMWF simulations, and CO_2 and CH_4 emission inventory and background concentration data. The CO_2 background concentration dataset was generously provided by Dr. Christine Groot Zwaaftink. Thanks to Dott. ric. Silvia Bucci for sharing code with me for the handling of FLEXPART-WRF's initial sensitivity files. I furthermore acknowledge Prof. Thomas Karl for supplying CO_2 and CH_4 concentration measurements taken at the University of Innsbruck. Meteorological ground observation data (TAWES) was obtained from GeoSphere Austria; radiosonde observations from the University of Wyoming. Moreover, I acknowledge the use of the CORINE land cover dataset for terrain classification.

The results presented have been achieved, in part, by utilizing computational resources of the Vienna Scientific Cluster (VSC).
I acknowledge the use of `cdo` (Climate Data Operators) functions for regridding and merging datasets. Furthermore, I want to gratefully acknowledge the use of helpful `python` libraries throughout my computations, such as: `numpy`, `pandas`, `xarray`, `matplotlib`, `cartopy`, `scipy.stats`, `geopandas`, `windrose`.

Lastly, as an expression of gratitude on a personal level, I want to acknowledge my Lord and Savior Jesus Christ for carrying me through every high and low throughout this project. Moreover, I am indebted to my wife Katia for her endless love, patience and encouragement for me. Also, I am immensely grateful for the support of my family, friends, and Pastor Philipp and the Revival Church family. Everyone's support means more to me than I can express.

Abstract

The presence of carbon dioxide (CO_2) and methane (CH_4) accounts for over 80% of atmospheric radiative forcing by greenhouse gases. While throughout the past decades much knowledge has been acquired on their sources and sinks (both anthropogenic and natural), as well as their global warming potential, a vast amount of research is carried out to gain insight on regional behavior of these species. In this study, the nation of Austria is considered.

Although global bottom-up emission inventory datasets (spatially disaggregated quantifications of source/sink activities) do exist, a refinement of accuracy and resolution of these, achieved by top-down methods, may be desired. Accurate computation of atmospheric transport is a substantial step towards improved top-down emission estimates. For this purpose, Lagrangian Particle Dispersion Models (LPDMs), such as FLEXPART (FLEXible PARTicle dispersion model), are commonly used. FLEXPART's trajectory computations are driven by meteorological input stemming from ECMWF (European Centre for Medium-Range Weather Forecasts) products, such as the ECMWF Reanalysis v5 (ERA5). However, understanding the behavior of greenhouse gases on smaller scales, particularly regions incorporating complex terrain, may require a model setup offering more flexibility on spatiotemporal resolutions (especially of its meteorological input). Thus, in this study, a different LPDM from the FLEXPART model family was employed to compute atmospheric transport of CH_4 and CO_2 - namely, FLEXPART-WRF, which receives meteorological information from the Weather Research and Forecast model (WRF).

Two objectives were pursued in this study. First, nine WRF model runs with 1km horizontal resolution and different properties concerning observation and grid nudging, and ERA5 reanalyses, were compared with ground observations, to assess their capabilities in reproducing the observed atmospheric state (and thus their suitability to serve as meteorological input for atmospheric transport modelling). Surface pressure, 2m temperature, and horizontal wind components, speed and direction were considered, and their Root Mean Square Errors (RMSE), Mean Absolute Errors (MAE), Pearson and Spearman correlations, as well as wind speed and direction distributions, were evaluated (all with respect to observations).

Grid nudging showed to be substantially more important to the overall performance of WRF than observation nudging, while the best results were achieved when combining the two. It was found that the most accurate WRF configurations represent 2m temperature and surface pressure more realistically than ERA5. Wind direction distributions tend to get improved by WRF, which also captured wind speed variability better than ERA5. However, with increasing station altitudes, WRF's performance suffered from overestimated wind speeds.

As a second objective of this study, FLEXPART-WRF's ability to reproduce measured

CO_2 and CH_4 concentration time series at all Austrian locations where these are available (Vienna, Innsbruck, Sonnblick) was investigated. FLEXPART-WRF was operated on a domain covering Austria, while FLEXPART-ECMWF simulations were conducted on a European domain, for a model period spanning 2022.
In Innsbruck, FLEXPART-WRF was able to reproduce observed concentrations of both CO_2 and CH_4 better than FLEXPART-ECMWF, reducing RMSEs by 24.89ppb (CH_4) and 8.1ppm (CO_2). At Sonnblick, the opposite was true; where FLEXPART-ECMWF's RMSEs were lower by 4.39ppb (CH_4) and 3.83ppm (CO_2), while improving correlations by over 35% for both species. In Vienna, FLEXPART-WRF matched observations better, but suffered from an overestimated baseline (by $\approx$50ppb) in CH_4 and a number of outliers in CO_2 simulations.
Furthermore, a bug in FLEXPART-WRF's computation of initial condition sensitivities on non-global domains was discovered, and a method of correction to the source code was proposed and implemented in this study.

Kurzfassung

Kohlendioxid (CO_2) und Methan (CH_4) sind verantwortlich für über 80% des von Treibhausgasen verursachten atmosphärischen Strahlungsantriebs. Obwohl in den letzten Jahrzehnten einiges Wissen über ihre Quellen, Senken (sowohl menschenverursacht, als auch natürlich) und ihr Treibhauspotential gewonnen wurde, findet viel Forschung statt, um tiefere Einblicke in das regionale Verhalten dieser Stoffe zu gewinnen. In dieser Studie wird Österreich betrachtet.

Trotz des Vorhandenseins von globalen bottom-up-Emissionsinventardatensätzen (räumlich aufgelöste Quantifizierungen von Quellen-/Senkenaktivitäten) ist eine Verfeinerung von deren Genauigkeit und Auflösung durch top-down-Methoden erstrebenswert. Ein wichtiger Schritt zu verbesserten top-down-Emissionsabschätzungen liegt in der akkuraten Berechnung von atmosphärischem Transport. Dafür werden häufig Lagrangesche Partikeldispersionsmodelle (LPDMs), wie beispielsweise FLEXPART (FLEXible PARTicle dispersion model), verwendet. FLEXPARTs Trajektorienberechnungen werden angetrieben von meteorologischen Eingangsdaten, die vom ECMWF (European Centre for Medium-Range Weather Forecasts) stammen, wie zum Beispiel die ECMWF Reanalysis v5 (ERA5). Um das Verhalten von Treibhausgasen auf kleineren Skalen zu verstehen, insbesondere in Regionen, die komplexes Terrain beinhalten, kann jedoch ein Modellsetup vonnöten sein, das flexibler bezüglich räumlicher/zeitlicher Auflösungen ist (speziell diejenigen des meteorologischen Inputs). Daher wurde in dieser Studie ein anderes LPDM aus der FLEXPART-Modellfamilie herangezogen, um den atmosphärischen Transport von CH_4 und CO_2 zu berechnen; nämlich FLEXPART-WRF, welches meteorologische Eingangsdaten vom Weather Research and Forecast model (WRF) erhält. Zwei Ziele wurden in dieser Studie verfolgt. Erstens wurden neun verschiedene WRF-Modellläufe mit 1km horizontaler Auflösung (und verschiedenen Eigenschaften hinsichtlich Observations- und Gitter-Nudging), sowie ERA5-Reanalysen, mit Bodenbeobachtungen verglichen, um ihre jeweilige Fähigkeit zur Nachbildung des atmosphärischen Zustandes (und somit ihre Eignung, als meteorologischer Input für atmosphärische Transportmodellierung zu dienen) festzustellen. Bodendruck, 2m-Temperatur, die horizontalen Windkomponenten (sowie -stärke und -richtung) wurden berücksichtigt, und ihre Root Mean Square Errors (RMSE), Mean Absolute Errors (MAE), Pearson- und Spearman-Korrelationskoeffizienten, sowie Windstärke- und Windrichtungsverteilungen, wurden evaluiert (alles davon mit Beobachtungen als Referenzwerte).

Grid-Nudging stellte sich als deutlich wichtiger für ein gutes Abschneiden von WRF heraus als Observations-Nudging, und die besten Resultate wurden mit der Kombination aus beiden erreicht. Es zeigte sich, dass die akkuratesten der WRF-Konfigurationen 2m-Temperatur und Bodendruck realistischer darstellen konnten als ERA5. WRF zeigte auch verbesserte Windrichtungsverteilungen sowie eine bessere Repräsentation der Vari-

abilität von Windgeschwindigkeiten. Mit zunehmender Stationshöhe hingegen litt das Abschneiden von WRF an einer Überschätzung von Windgeschwindigkeiten.
Als zweites Ziel dieser Studie wurde die Fähigkeit von FLEXPART-WRF untersucht, Konzentrationsmessungen von CO_2 und CH_4 an jenen österreichischen Standorten, wo diese vorhanden sind (Wien, Innsbruck, Sonnblick), zu reproduzieren. Für einen Modellzeitraum über das Jahr 2022 rechnete FLEXPART-WRF auf einem das Land Österreich abdeckenden Areal, und FLEXPART-ECMWF-Simulationen fanden auf einem europäischen Bereich statt.
Am Standort Innsbruck konnte FLEXPART-WRF die beobachteten CO_2- und CH_4-Konzentrationen besser reproduzieren als FLEXPART-ECMWF, wobei sich der RMSE um 24.89ppb (für CH_4) sowie um 8.1ppm (für CO_2) reduzierte. Ein gegenteiliger Effekt war beobachtbar am Sonnblick, wo FLXPART-ECMWFs RMSEs um 4.39ppb (CH_4), beziehungsweise 3.83ppm (CO_2), niedriger lagen, wobei sich gleichzeitig für beide Gase die Korrelationen um über 35% höher zeigten. In Wien stimmte FLEXPART-WRF besser mit Messungen überein, aber seine Ergebnisse litten für CH_4 unter um ungefähr 50ppb überschätzten Hintergrundkonzentrationen und unter einigen Ausreißern für CO_2.
Des Weiteren wurde eine Fehlfunktion in FLEXPART-WRFs Berechnungen von der Sensibilität von Konzentrationen zu Anfangsbedingungen auf nicht-globalen Bereichen entdeckt - in dieser Studie ist hierfür eine Methode zur Korrektur vorgeschlagen und umgesetzt.

Contents

1. Introduction

1.1. Context

Presently, a vast range of research endeavors is taking place globally, investigating the life cycles, emissions and sinks, distributions, radiative forcing potentials and climate impact of greenhouse gases in the atmosphere [Grubb et al., 2023]. Atmospheric concentrations and dispersion of certain greenhouse gases (GHGs) are strongly dependent on human activity, the most important anthropogenically influenced species being carbon dioxide (CO_2) and methane (CH_4) [EPA].
It can be shown that the primary anthropogenic sources of CO_2 in the atmosphere (besides natural sources, such as wildfires, etc.) are combustion of fossil fuels, as well as land use change (like deforestation), while the most prevalent sinks consist of carbon and oceanic sinks [Le Quéré et al., 2009].
Similarly, it can be noted that the major sources of atmospheric CH_4 are comprised of those that are natural (such as natural wetlands and organic waste), as well as anthropogenic ones (combustion of coal, oil, natural gas and biomass, as well as agricultural livestock emissions), whereas sinks are mainly of chemical nature (reactions in the atmosphere, primarily with the hydroxyl (OH) radical) [Kirschke et al., 2013]. It is noteworthy, though, that even natural sources may be influenced by human activity, such as surface changes by direct action (e.g. land use changes, drainage of wetlands, etc.), or surfaces changing indirectly, by the consequences of rising temperatures.
Moreover, despite ongoing efforts unto reduction of emissions of greenhouse gases, observations show that global concentrations of CO_2 and CH_4 are still on the rise [Zhang et al., 2023], [Shindell et al., 2024]. While on large scales the radiative forcing potentials of such species, as well as their distributions, are well-known [Kenawy et al., 2023], [Raghuraman et al., 2023], there are, however, aspects about these gases that have been less investigated and therefore have remained more open questions thus far. These include:

- What are sources and distributions of these species on regional scales?
- What are behavior patterns of greenhouse gas dispersions in complex/mountainous terrain?
- And, how about our capabilities to model these, as well as the corresponding concentrations, in said complex terrain?

This is important, as current research on greenhouse gas emissions states that "additional studies focused on discrepancies between bottom-up and top-down emissions on smaller area are needed" and a "tendency to make inventories with higher spatial

resolution is evident" [Dolšak Lavrič et al., 2023].
In contrast to conventional bottom-up emission inventories (which comprise information about emissions, based on knowledge about the activity of known sources and sinks), "global, regional and national GHG emissions can be estimated using atmospheric measurements and atmospheric models (the "top-down" approach). This approach links emissions with atmospheric concentrations using atmospheric transport (and chemistry) models and is often referred to as "inverse modelling"." [Bergamaschi et al., 2018].
A specific example for an inverse modelling framework is described in [Thompson and Stohl, 2014], by which a priori knowledge about emission patterns of a certain species (obtained by bottom-up inventories) gets updated and improved in a Bayesian manner by numerical modelling of the atmospheric transport of particles, employing a so-called Lagrangian Particle Dispersion Model (LPDM), from which the likelihood that emissions arriving at a certain receptor site stem from certain regions can be concluded.
Such LPDMs (a summary of the way these models function can be found in Section 2.1), computing particle dispersion, which is mainly driven by wind, make up the state-of-the-art approach to modelling atmospheric transport of various trace gases and aerosols. One of the most common models of this kind is the FLEXible PARTicle dispersion model (documented in [Stohl et al., 1998], [Stohl et al., 2005], [Pisso et al., 2019], [Bakels et al., 2024], etc.). It has been widely used for a number of applications, e.g. modelling transport and distributions of airborne microplastic [Bucci et al., 2024], ash at volcanic eruption events [Moxnes et al., 2014], radionuclides [Stohl et al., 2012], particulate matter such as dust aerosols [Groot Zwaaftink et al., 2017], greenhouse gases [Bergamaschi et al., 2022], as well as atmospheric heat and moisture transport [Baier et al., 2022] (this list is not comprehensive and merely serves to provide examples).

While FLEXPART is typically driven by meteorological fields that are available on a global scale, there exists a branched-off version which is driven by input from the Weather Research and Forecasting model (WRF) [NCAR], known as FLEXPART-WRF (documented by [Fast and Easter, 2006], [Brioude et al., 2013]). As WRF model simulations can be run at spatial (and temporal) resolutions finer than those common to global state-of-the-art NWP (numerical weather prediction) models and reanalyses, FLEXPART-WRF, for its computation of atmospheric transport, is able to utilize this finer resolved meteorological input information (which may be desirable for the conduction of studies on more regional scales).

1.2. Motivation

In the nation of Austria, specifically, thorough coverage and availability of greenhouse gas concentration measurements does not exist. This is why this study aims to provide first steps in developing methods building up to a potential future inverse modelling framework, in order to conduct comprehensive top-down estimation studies (as e.g. done on a global scale by [Vojta et al., 2022]) for CO_2 and CH_4 dispersions over smaller scales (a domain spanning Austria).

Furthermore, Austria contains a substantial part of the Alps, with around 60% of the nation being covered by mountainous areas [van der Maaten-Theunissen et al., 2013], and thus possesses complex terrain, which generally challenges the performance of numerical geoscientific models [Rontu, 2013], [Brioude et al., 2012]. Therefore, this study seeks to investigate whether refining the resolution of meteorological data driving atmospheric transport models increases the quality of dispersion simulations of species like CO_2 and CH_4 in such terrain.
To achieve this, as a first step, it has to be shown that by the use of such a finer resolved transport modelling setup (in this study provided by the use of the FLEXPART-WRF LPDM), observed greenhouse gas concentrations can be reproduced better than by conventional (more coarsely resolved) setups (i.e. classical FLEXPART-ECMWF, using global meteorological input fields) at those few Austrian locations where measurements are available (namely, Innsbruck, Sonnblick and Vienna).
Thus, for this purpose, in the scope of this study, the following research questions are anticipated to be answered:

1. *Can an atmospheric transport modelling setup with a spatial resolution finer than conventional methods (using the example of FLEXPART-WRF) successfully reproduce CO_2/CH_4 concentration measurements in Alpine terrain?*
2. *How well can said setup tackle typical challenges of atmospheric transport modelling, such as dealing with small scales and orography?*

2. Methods

2.1. The FLEXPART Model

FLEXPART is a so-called Lagrangian Particle Dispersion Model (LPDM), which stands in contrast to Eulerian dispersion models. While Eulerian models seek to directly solve the governing advection-diffusion equation on a 4D spatiotemporal grid, yielding the net effect of all particles and relevant processes they are subject to in each grid cell, LPDMs generate numerical "particles", whose trajectories are computed individually, according to the pertinent equations [Nordam et al., 2023], [Xu et al., 2020].
The FLEXPART model incorporates numerical computations of various processes of relevance to atmospheric transport. These include transport by advection, turbulence, dry and wet deposition, radioactive decay, and chemical reactions that can be represented by a linear scheme, such as the hydroxyl (OH) radical reaction [Pisso et al., 2019].

The set of particle transport equations implemented in FLEXPART to compute the motion of each particle is given by [Stohl et al., 2005] as

$$\boldsymbol{X}(t+\Delta t) = \boldsymbol{X}(t) + \boldsymbol{v}(\boldsymbol{X}, t)\Delta t, \tag{2.1}$$

$$\boldsymbol{v} = \overline{\boldsymbol{v}} + \boldsymbol{v_t} + \boldsymbol{v_m}, \tag{2.2}$$

$$dv_{t_i} = a_i(\boldsymbol{x}, \boldsymbol{v_t}, t)dt + b_{ij}(\boldsymbol{x}, \boldsymbol{v_t}, t)dW_j. \tag{2.3}$$

In this equation system, Equation (2.1) describes a linear approximation of the trajectory equation, where t denotes time, Δt a time increment, and $\boldsymbol{X}$ the vector of spatial position.
$\boldsymbol{v}$ represents the wind vector, which, as noted in Equation (2.2), comprises three components - the grid-scale wind $\overline{\boldsymbol{v}}$, combined with mesoscale fluctuations $\boldsymbol{v_m}$ and turbulent fluctuations $\boldsymbol{v_t}$. The components i of $\boldsymbol{v_t}$ get computed according to the Langevin equation (Equation (2.3), [Thomson, 1987]), in which a_i and b_i denote spatially dependent drift and diffusion terms, and dW_j represents components of a Wiener process [Legg and Raupach, 1982], which corresponds to random noise increments with mean 0 and variance dt.

FLEXPART is capable of modelling forward in time, as well as backward. Whenever the number of sources of emissions of the considered particle species is assumed to exceed the number of receptors of interest, it is recommended to operate FLEXPART in backward mode. By that, backtrajectories of virtual particles are computed in negative temporal direction from a chosen receptor location.
Though FLEXPART, being a Lagrangian model, does not compute particle transport on a grid (as done in Eulerian models) but along trajectories, the model output is (in most

cases) written into a spatiotemporal grid of chosen resolution nonetheless. This model output contains a so-called emission sensitivity function (with the unit of seconds), which corresponds to a combination of the total residence time of the particles in each grid cell (as they follow their respective trajectories), and an account for the loss processes mentioned above [Stohl et al., 2005], [Pisso et al., 2019]. The name of this function is derived from the understanding that if particles traced back from a receptor site spend much time in a certain grid cell, the receptor site is proportionally "sensitive" to emissions that may potentially happen in this grid cell at that time.

2.1.1. Interfacing FLEXPART Output with Emissions

The described FLEXPART backward simulations, computing backtrajectories from a chosen receptor site and point of time, can be used to obtain source contribution maps. This spatiotemporal data reveals where emissions of the modelled species (e.g. a greenhouse gas) occurred in the past that contribute to the concentration of that same species at the time at which the backtrajectories were launched. To achieve this, FLEXPART model output needs to be coupled with emission inventories. Such datasets commonly contain information about emissions (source and sink activity) of certain species, taking place on a certain geographical domain, and are usually given in mass flux units (mass per time and area; e.g. $\mathrm{kgm^{-2}s^{-1}}$). (The emission inventory datasets utilized in this study are described in Section 2.1.4.) Solely based on a dataset like this, though, it cannot be known which geographical regions' emissions impact concentrations at the receptor location at a specific point of time t_0.
However, emission sensitivity functions resulting from FLEXPART simulations highlight to which areas' emissions a receptor site would be sensitive at a certain time. Thus, combining emission sensitivities with bottom-up emission inventory estimates yields a map of source region contributions to the concentration of the species of interest at the receptor location.
Furthermore, since emission inventories contain surface emission fluxes, while the emission sensitivity function describes the receptor location's sensitivity to volume fluxes into the lowest FLEXPART model layer, the surface fluxes need to be divided by the depth of this layer. Thus, source contributions SC (with $[SC] = \mathrm{kgm^{-3}}$) are obtained, as described in Equation (2.4):

$$SC(i,j,t_0) = \frac{1}{\Delta z_1} \cdot \sum_{t=t_0-t_B}^{t_0} ES(i,j,t) \odot EI(i,j,t). \tag{2.4}$$

$SC(i,j,t)$ denotes the field of source contributions to concentrations at the receptor site, $ES(i,j,t)$ the lowest model level of FLEXPART emission sensitivities (where $[ES] = \mathrm{s}$), and $EI(i,j,t)$ (with $[EI]$ assumed as $\mathrm{kgm^{-2}s^{-1}}$) the fluxes given by the bottom-up emission inventory dataset; all spatially dependent on the horizontal and vertical number of grid cell (i,j). Δz_1 denotes the depth of FLEXPART's lowest model layer (depending on user choice). The model time variable t is discrete and resolved in steps Δt. Let t_0 be one specific model time step. t_B represents the backtrajectory time, i.e. the length of

the time span for which trajectories are computed/followed backward by FLEXPART, and is an integer multiple of Δt. The Schur product $\odot$ describes an element-wise matrix multiplication. Thus, for each modelled backward time step, the emission sensitivity field gets multiplied with the emissions taking place according to the emission inventory, and all the backward time steps leading up to t_0 get summed up.
Therefore, the resulting fields, computed for each FLEXPART output time step, depict spatial maps of past emissions (with respect to the considered time step t_0; taking place between $t = t_0 - t_B$ and $t = t_0$, respectively), that are contained in the emission inventory dataset, that (highlighted by FLEXPART backtrajectories) contribute to the concentration value at the receptor location at $t = t_0$.

In order to verify results of FLEXPART simulations, they need to be compared with existing measurements of atmospheric concentrations of the considered species. Since such measurements conventionally are available as time series, it is imperative to compute a time series from the model output. at the FLEXPART simulation location
To obtain such a time series of the atmospheric concentration C of a modelled species at a receptor location, the source contribution maps present for each modelled time step, resulting from Equation (2.4), need to be spatially integrated. This can be expressed by Equation (2.5).

$$C(t_0) \;=\; \phi_s \cdot \sum_{i=0}^{n_x} \sum_{j=0}^{n_y} SC(i,j,t_0) \;+\; C_B(t_0). \tag{2.5}$$

In this equation, $C(t_0)$ represents the modelled concentration at time step t_0, $SC(i,j,t_0)$ is the pertaining field of source contributions obtained by Equation (2.4), (i,j) denote counter variables for grid cells in x and y direction (where n_x and n_y are the total numbers of grid cells of the model domain in x and y direction), and ϕ_s is a unit conversion factor depending on the species s (which is responsible for yielding C in the desired unit). The term $C_B(t_0)$ describes the amount of ambient background concentration of the considered species, and its meaning and computation are described in Section 2.1.2.
Looking at the first term in Equation (2.5) (and disregarding the unit conversion factor ϕ_s), the result of the summation over x and y remains in the unit kgm^{-3} (since this is also the unit of SC) - the one commonly associated with mass concentrations.

While in some cases this may be the desired unit for concentrations, in this study, the species considered (the greenhouse gases CO_2 and CH_4) are conventionally measured in ppm (particles per million) and ppb (particles per billion), respectively. This raises the necessity of defining the unit conversion factors ϕ_s for the species $s = CO_2$ and $s = CH_4$ in the following way:

$$\phi_{CO_2} \;=\; 10^6 \frac{k_b T(t_0)}{p(t_0)} \frac{N_A}{M_{CO_2}}, \tag{2.6}$$

$$\phi_{CH_4} \;=\; 10^9 \frac{k_b T(t_0)}{p(t_0)} \frac{N_A}{M_{CH_4}}. \tag{2.7}$$

In Equation (2.6), $p(t_0)$ and $T(t_0)$ are surface pressure and 2m temperature at the receptor location at time t_0, $k_B = 1.38 \cdot 10^{-23}\,\mathrm{m^2kgs^{-2}K^{-1}}$ denotes the Boltzmann constant, $N_A = 6.2 \cdot 10^{23}$ the Avogadro constant, and $M_{CO_2} = 0.044\,\mathrm{kgmol^{-1}}$ the molar weight of CO_2.
There are multiple steps encompassed in this formula for the conversion from $\mathrm{kgm^{-3}}$ to ppm. Firstly, one can convert from the present mass (kg) per volume ($\mathrm{m^3}$) to the mass per million particles. Thus, a normalization from the total particle number present in a cubic meter to the particle number of a million needs to be done, employing a normalization factor of $\frac{10^6}{N}$ (with N being the number of particles in a cubic meter). According to the ideal gas law $pV = Nk_BT$, the normalization factor becomes $\frac{10^6}{N} = 10^6 \frac{k_BT(t_0)}{p(t_0}$, receiving $p(t_0)$ and $T(t_0)$ from measurements of pressure and temperature at the receptor location at time t_0 (V vanishes, since the considered volume is $1\,\mathrm{m^3}$). The last remaining conversion step - from kilograms per million particles to the dimensionless ppm - is performed by dividing the result of the previous step by the mass that one single molecule of CO_2 carries, which is given by $\frac{M_{CO_2}}{N_A}$ (i.e. the molar mass of CO_2 divided by the number of particles contained in 1 mol, namely N_A); thus completing the expression in Equation (2.6).

Except for two minor adjustments, the steps taken to obtain Equation (2.7) are fully analogous. Said adjustments show firstly in the use of a factor of 10^9 in place of 10^6, since CH_4 concentrations are conventionally measured in ppb instead of ppm; and secondly, the molar weight of CH_4 (being $M_{CH_4} = 0.016\,\mathrm{kgmol^{-1}}$) must be used instead of the one of CO_2.

2.1.2. Interfacing FLEXPART Output with Initial Conditions

As seen in Equation (2.5) there is another component to consider when computing concentration time series from FLEXPART model runs - namely, the background concentration term C_B.
Since FLEXPART traces back particle trajectories only by a user-chosen time span t_B, the first term in Equation (2.5), for each time step t_0, only accounts for emissions taking place in the time interval $t_0 - t_B < t < t_0$. While for some atmospheric trace gases and aerosols this may yield an accurate concentration estimate at the receptor location, as soon as the atmospheric lifetime of the considered species approaches the time span t_B (which conventionally is chosen to be within a range of a few days up to a few weeks), emissions of that species taking place in that time window constitute only a fraction of the total measurable concentration - the other fraction consisting of ambient background concentrations present in a well-mixed atmosphere. CO_2 and CH_4, the species considered in this study, are both known to be longer-lived than typical choices of t_B by many orders of magnitude [Archer et al., 2009], [Lelieveld et al., 1998]. Therefore, to obtain a modelled concentration time series which is comparable with observations, it is inevitable to take these background concentrations into account.
(An estimate of these concentrations can be obtained e.g. by long-term forward model

runs of FLEXPART.)

Noticing this, it can thus be said that for these species, the simulated concentration at the receptor location at time t_0 depends on two components: Firstly, on emissions occurring along the simulated trajectories in the time window between $t_0 - t_B$ and t_0; and secondly, on background concentrations at the time $t_0 - t_B$ (when the backward simulation is completed) in the regions where the trajectories get terminated (these background concentrations can be understood as "initial conditions" of the simulation). In FLEXPART, there exists an option to compute and write out - additionally to the regular model output - a field of sensitivity values to these initial conditions. In other words, for one specific time step t_0, this field contains information about regions to whose background concentrations at the time when particle trajectories are fully modelled backwards (i.e. the time $t_0 - t_B$), the concentration at time t_0 at the receptor location is sensitive. These initial condition sensitivity fields possess the same spatial resolution (horizontally and vertically) as the regular FLEXPART output.
Thus, the background concentration contributions $C_B(t_0)$ to the total concentration $C(t_0)$ at the receptor location at time t_0 can be obtained by:

$$C_B(t_0) = \sum_{i=0}^{n_x} \sum_{j=0}^{n_y} \sum_{k=0}^{n_z} IS(i,j,k,t_0 - t_B) \odot c_B(i,j,k,t_0 - t_B), \tag{2.8}$$

where IS denotes the initial condition sensitivity described above, c_B is a field of background concentrations of the species of interest (in the same spatial resolution as FLEXPART output); and after element-wise multiplication of these two fields, the triple sum represents spatial integration, where n_x, n_y, n_z are the number of grid points in the respective dimensions.

Having discussed all the ingredients used in simulations of concentration time series with FLEXPART, the typical workflow of such an LPDM to obtain a simulated greenhouse gas concentration time series is summarized in the schematic Figure 2.1.

2.1.3. The FLEXPART-WRF Model

In this study, two versions of FLEXPART were employed in backward mode to assess their respective capabilities to model greenhouse gas concentration time series in complex terrain. Simulations were carried out with FLEXPART-WRF 3.3.1 (as described in [Brioude et al., 2013]), which is forced by input fields stemming from the WRF meteorological model [NCAR], as well as the more conventional FLEXPART-ECMWF [Pisso et al., 2019], which utilizes ECMWF (European Centre for Medium-Range Weather Forecasts) products, such as ERA5 (ECMWF Reanalysis v5) reanalyses [Hersbach et al., 2020], as meteorological input. While these two LPDMs exhibit minor differences (which can mainly be traced back to the differences in input data handling; e.g. working with various map projections possible in WRF), the aforementioned principles (such as the coupling with emissions and initial conditions) described in the preceding sections hold for both versions. Two

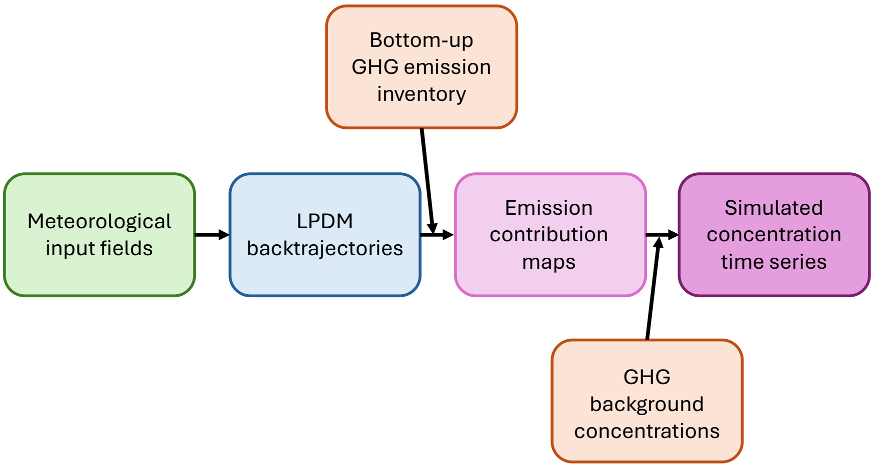

Figure 2.1.: The typical workflow of an LPDM like FLEXPART to generate simulated greenhouse gas concentration time series at any receptor location. Meteorological input data is utilized as forcing for the LPDM computation of particle backtrajectories. Results of these simulations get coupled with bottom-up emission inventories to obtain maps of surface emission contributions to the simulated concentrations (as described in Section 2.1.1). Initial condition sensitivity information, also provided by the LPDM, is interfaced with background concentration information of the species of interest (see Section 2.1.2), to determine the contribution of ambient concentration levels to the concentration at the receptor location. Adding these two yields the complete simulated time series.

exemplary differences are described as follows.
First, a notable property of FLEXPART-WRF is the possible use of time-averaged and mass-weighted components of the wind vector, as this quantity is available from WRF simulations. The use of these wind variables is intended to better represent (than instantaneous snapshot wind values) ongoing atmospheric motion throughout a certain time interval, thus allowing for a more accurate quantification of particle transport, which is mainly driven by wind. Moreover, FLEXPART-WRF in the referenced version was capable already of parametrizing turbulence such that vertical velocity values satisfy a skewed probability distribution instead of a Gaussian. This represents vertical velocity distributions under convective conditions much better than a standard Gaussian model [Stohl et al., 2005]. While this feature distinguished FLEXPART-WRF from FLEXPART-ECMWF at the time of its release, it subsequently got implemented therein as well.

2.1.4. Datasets and Model Settings

Emission Inventories & Background Concentrations

As described in Section 2.1.1, FLEXPART(-WRF) model output needs to be coupled with prior bottom-up emission information, usually in the form of emission inventory datasets.
To model CO_2 concentrations, for the description of anthropogenic and wildfire emissions, data provided by the Copernicus Atmosphere Monitoring Service (CAMS) was used. The anthropogenic component on the nested domain stems from the CAMS-ANT-REG dataset [CAMS-ANT-REG], processed with the High-Elective Resolution Modelling Emission System version 3 (HERMESv3) [Guevara et al., 2019], and the fire emission component from the CAMS-GFAS product [CAMS-GFAS], [Kaiser et al., 2012]. Biospheric emission fluxes are based on a Vegetation Photosynthesis and Respiration Model (VPRM) dataset [Glauch et al., 2025]. To account for emission fluxes outside of the nested European domain of FLEXPART-ECMWF, the same dataset was used for the wildfire component, CAMS-ANT-GLOB for the anthropogenic contribution [CAMS-ANT-GLOB], [Granier et al., 2019] (similar to the regional product mentioned above), while biospheric fluxes were estimated by the Lund-Potsdam-Jena General Ecosystem Simulator (LPJ-GUESS) [Wu et al., 2024]. Furthermore, oceanic CO_2 exchange was accounted for by data from the Surface Ocean CO_2 Atlas (SOCAT) [CarboScope], [Rödenbeck et al., 2022].
CO_2 background concentrations were obtained from Christine Groot Zwaaftink.
For CH_4 simulations, the anthropogenic emission contribution again stems from CAMS-ANT-REG CAMS-ANT-REG. Further components considered are wetlands [Bloom et al., 2021], wildfires [RANDERSON et al., 2017], the geological component [Etiope et al., 2019], oceanic exchange [Weber et al., 2019], as well as the soil sink [Ridgwell et al., 1999]. Background concentration data of CH_4 originates from [Groot Zwaaftink et al., 2018].

Austrian Greenhouse Gas Concentration Observations

Measured CO_2 and CH_4 time series from the three available locations in Austria served as observational "truth" to compare FLEXPART-WRF and FLEXPART-ECMWF model results to. Observations in Innsbruck were supplied by Thomas Karl from the University of Innsbruck. For Sonnblick, the greenhouse gas concentration dataset from Sonnblick Observatory was utilized [Sonnblick-Observatorium]. Concentration measurements in Vienna stem from the Vienna Urban Carbon Laboratory (VUCL) project [Matthews and Schume, 2022], conducted at Arsenal tower.

FLEXPART-WRF and FLEXPART-ECMWF Model Settings

FLEXPART-WRF, according to the coverage of WRF simulations, was run in backward mode on an Austrian domain (see Figure 2.2), whereas FLEXPART-ECMWF simulations were conducted globally (1°×1° spatial resolution), including a nested domain covering Europe. Both models' simulations were conducted at the three Austrian locations where greenhouse gas concentration measurements are available: Innsbruck University, Sonnblick

Table 2.1.: Settings of the FLEXPART-WRF and FLEXPART-ECMWF (nested domain) model runs.

Property	*FLEXPART-WRF*	*FLEXPART*
Extent	8.2-18.7°E, 45.5-49.5°N	CH_4: -15-35°E, 35-72°N CO_2: -10.5-34.75°E, 35-71.75°N
Horizontal resolution	0.01°×0.01°	0.25°×0.25°
Vertical levels (m)	5, 10, 50, 100, 250, 500, 700, 900, 1000, 1250, 1500, 1750, 2000, 3000, 4000, 5000, 7500, 10000	CO_2: 100, 500, 1000, 2000, 3000, 5000, 7000, 9000, 12000, 15000, 20000, 50000 CH_4: 100, 250, 500, 750, 1000, 1500, 2000, 2500, 3000, 3500, 4500, 5000, 5500, 6500, 7000, 7500, 8500, 9000, 9500, 11000, 12000, 13000, 15000, 17000, 19000, 20000, 21250, 23750, 26250, 28750, 32500, 37500, 42500, 47500, 50000
Temporal resolution	1h (releases & output)	3h (releases & output)

observatory, and Vienna Arsenal tower.
The properties of the FLEXPART-WRF domain, as well as of the nested FLEXPART-ECMWF domain, are listed in Table 2.1. While FLEXPART-ECMWF simulations were computed with a backward simulation time of $t_B = 10$ days, in FLEXPART-WRF $t_B = 2$ days proved sufficient, due to the majority of particles leaving the simulation domain within this time.

2.1.5. The Initial Condition Issue in FLEXPART-WRF

The standard procedure of coupling FLEXPART backward model runs with ambient concentration information, serving as initial conditions, is described in Section 2.1.2. However, it showed while performing FLEXPART-WRF simulations for this project, that this feature, for use cases with limited spatial domains, unfortunately seems to be implemented incorrectly (FLEXPART-WRF 3.3.1). An description of this bug follows below.

IS, the three-dimensional sensitivity function to background concentrations, as described in Section 2.1.2, receives its values from every individual trajectory of each simulated particle at completed backward simulation time. These sensitivity values are clearly linked to the respective trajectory positions at that time, meaning: If many trajectories are terminated in the same vicinity at the end of the backward simulation, this simulation is highly sensitive to background concentrations of the species of interest in that area.
Once a trajectory is terminated, the initial sensitivity value caused by this trajectory

is computed and dumped into the IS matrix. For simulations which do not cover a global spatial domain though, trajectories need to not only be terminated at the time of simulation end, but also once particles leave the domain. Thus, an accumulation of initial condition sensitivity at the domain boundaries would be expected. The IS field contains merely one temporal snapshot, which represents the model time at completion of the backward simulation (described as $t_0 - t_B$ in Equation (2.8)). Therefore, assigning initial sensitivities generated by trajectories that are terminated by leaving the domain before simulation completion to that same timestamp would introduce an error (which is unavoidable, since the IS output is not fashioned to contain different time steps). However, since ambient background concentrations of species that are long-lived enough to even necessitate their consideration do not underlie large fluctuations on the backward simulation time scales of this study (t_B =2d; see Section 2.1.4), this error of temporal mismatch is neglected.

In the use of any version of FLEXPART on a very limited spatial domain (as in this study; shown in Figure 2.2) it is a common occurence for particles to leave the domain quickly. Unfortunately, it seemed as though in FLEXPART-WRF 3.3.1, particles leaving the domain do not get terminated once they leave the domain, and therefore, initial sensitivity information does not get dumped in the initial sensitivity matrix, which corrupts the information needed for coupling simulations with background concentrations. This poses a huge systematic error in simulating greenhouse gas concentration time series, due to the contribution of the ambient background to momentary concentration values (for species considered in this study) being at least four to five times as large as any source's emission contributions - anthropogenic or natural - taking place within the simulation time window.
(Remark: Particles leaving the domain do not get terminated in FLEXPART-ECMWF either, which also showed while undertaking simulations for this study. There, however, this issue can be easily circumvented by simulating on a global and nested domain, and coupling the initial conditions with the global IS output. As opposed to WRF's limited-domain coverage in this study, ERA5 is a global dataset, and therefore allows for this approach in FLEXPART.)
Upon investigation of the source code of FLEXPART-WRF 3.3.1, it became visible that an attempt of implementation of the termination of trajectories at the domain boundaries was present. However, in that section of the code, the termination is set to happen once the trajectory would leave the mother grid of the WRF meteorological input (instead of once the particle position goes beyond the FLEXPART-WRF simulation grid). Leaving the mother domain, obviously, would only happen after a departure from the FLEXPART-WRF simulation domain, since the WRF grid needs to extend at least as far as the FLEXPART-WRF grid (in order to supply meteorological information on the whole FLEXPART-WRF domain).
Thus, in this study, the source code of FLEXPART-WRF 3.3.1 got edited accordingly and the modified version was used for all simulations. The modification process of the source code happened as follows:

(Please note that the edit is currently only fashioned to work for FLEXPART-WRF output grids that are defined in degrees of longitude/latitude!)

1. A variable called `fringewidth` got introduced to the user input file of FLEXPART-WRF and declared in the program `com_mod.f90`, where all common variables get declared.
   (Remark: For a currently unknown reason, initial sensitivity information may "travel" further than the location of trajectory termination. Therefore, it showed to be insufficient to just terminate trajectories at the domain boundaries - IS information would still get lost. Thus, it becomes necessary to force termination at a certain margin within the domain, so that as much of the remaining IS information as possible, which is dumped thereafter, still remains in the FLEXPART-WRF domain, in order to be available to use in postprocessing.)
   The `fringewidth` variable determines the width of the margin spanning from the domain boundaries inwards, within which trajectories are to be terminated (as seen by the green and turquoise box in Figure 2.2). Its unit is a number of grid cells, meaning, if, like in this study, a grid cell spans 0.01°x0.01° and `fringewidth` $= 50$, the margin width would amount to 0.5° in longitude and latitude direction.

2. For the model to receive the `fringewidth` value as specified by the user in the input file, a `read` command for its ingestion needed to be added into the subroutine `readinput.f90`.

3. The time integration of each trajectory is carried out in the subroutine `advance.f90`. If any trajectory gets terminated, `advance.f90` sends this information back to the main program. Thus, it is necessary to implement the termination condition in the loop iterating over each particle - namely, whenever some particle gets closer to the domain boundary than the number of grid cells specified by `fringewidth`, the termination marker is set.
   (Remark: Since the domain extent is given in degrees longitude and latitude, and particle positions throughout the time integration get handled in the "xy index" coordinate system native to FLEXPART-WRF, the subroutine `xyindex_to_ll_wrf_out.f90` needs to be utilized for coordinate transformations.)

4. Though the improvement achieved by this procedure is drastic (see Section 3.2.1), a small fraction of information leaves the domain nonetheless (as stated above). In some use cases, like this study - dealing with greenhouse gases -, the background concentrations of a species may by far be the biggest contributor to the total concentration, such that even a few-percent fluctuation thereof would introduce large errors to the results. This may therefore necessitate a normalization of the initial sensitivity fields' integral to 1.

Table 2.2.: Properties of the nine different WRF configurations, in attempting to find which one reproduces meteorological observations best.

Name	*Observation nudging*	*Grid nudging*	*Other*
`em_real_five_obs_grid_nudg`	1h, 5km	3h	-
`em_real_five_obs_grid_nudg1h`	1h, 5km	1h	-
`em_real_five_obs_nudg`	1h, 5km	-	-
`em_real_no_obs_nudg`	-	3h	-
`em_real_no_obs_grid_nudg`	-	-	-
`em_real_no_obs_grid_nudg_Dudhia`	-	-	Dudhia shortwave radiation scheme
`em_real_five_obs_grid_nudg1h_twnd`	1h, 5km	1h	`topo_wind=1`
`em_real_five_obs_nudg_20k`	1h, 20km	-	-
`em_real_no_obs_nudg1h`	-	1h	-

2.2. Meteorological Input for the FLEXPART models

With the purpose of making a case for the use of FLEXPART-WRF for the simulation of greenhouse gas concentrations over complex terrain, it is imperative to assess how well the meteorological input for this model represents "reality" (estimated by observations) compared to the input of FLEXPART-ECMWF.

As mentioned above, FLEXPART-ECMWF utilizes ERA5 reanalysis data as meteorological information, whereas FLEXPART-WRF uses data stemming from WRF simulations. While ERA5 works on a horizontal resolution of 31km and hourly temporal frequency [Hersbach et al., 2020], WRF, if configured accordingly, serves as a much more flexible source of meteorological information, also being capable of finer spatial (and temporal) resolutions. This is particularly crucial for dealing with domains including complex terrain with many small-scale variations, such as alpine regions (as investigated in this study). To harness this flexibility as best as possible, different WRF configurations, which are described in the following section, were tested and compared.

2.2.1. The WRF Configurations

Nine configurations of WRF were compared with ERA5 and ground observations at locations in the simulation domain, to assess which meteorological model represents observed "reality" best. The used WRF configurations all possess a horizontal resolution of 1km in x and y directions and 110 vertical levels; as well as a 10 minute temporal resolution. In Figure 2.2, the spatial extent of the domain can be seen.
Nudging and other properties of the specific configurations are described in Table 2.2.

In the nine mentioned configurations in Table 2.2, observation nudging, happening at the temporal frequencies and within the radii around the assimilated stations as mentioned, utilizes ground observations from the TAWES network [GeoSphere], which consists of about 270 semi-automated measurement stations all over Austria. Grid nudging happens

towards ERA5 data at temporal frequencies as listed.
The `em_real_no_obs_grid_nudg_Dudhia` configuration employs a non-default scheme for shortwave radiation transfer. In `em_real_five_obs_grid_nudg1h_twnd`, effects of subgridscale orography on wind are parametrized [Jimenez and Dudhia, 2012].

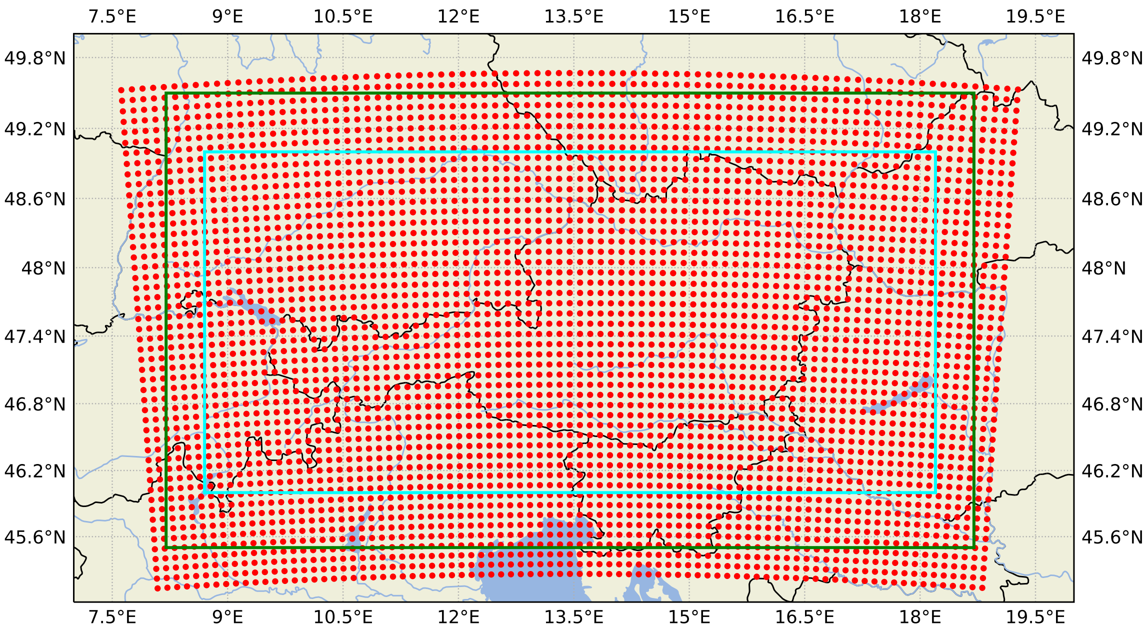

Figure 2.2.: Simulation domains of the nine WRF configurations in Table 2.2 (red dots at every tenth grid point) and FLEXPART-WRF (green and turquoise boxes), covering Austria. The turquoise box depicts the domain without (and the green box with) the margin set by the `fringewidth` parameter introduced to FLEXPART-WRF in this study (as described in Section 2.1.5).

2.2.2. Observational Data

In order to find which one of the aforementioned configurations of WRF represents the state of the atmosphere best (and to investigate whether any represents it better than ERA5 reanalyses, respectively), they were compared to surface observations. For this purpose, observational data from the TAWES network [GeoSphere2] was used as a reference.
This dataset is the first version of hourly values measured by the approximately 270 semi-automatic in-situ surface observation stations all throughout Austria. Hourly values of surface pressure and 2m temperature represent instantaneous measurements; hourly values of wind speed and direction are obained by vectorial averaging of six preceding measurements in ten-minute frequency.

2.2.3. Evaluation of the Performance of Meteorological Data

To evaluate the performance of different sources of meteorological information (namely, ERA5 reanalyses and the nine WRF configurations introduced in Section 2.2.1), they all got validated against TAWES observational data, which serves as an approximation for the "true" state of the atmosphere at the locations at which it is available.
The quantities that were evaluated are the ones most relevant for modelling of atmospheric transport - namely wind (components, speed and direction), temperature and pressure. All metrics used for the evaluation are described in Section 2.2.4.

In some of the WRF configurations, TAWES data was assimilated in the observation nudging scheme (according to Table 2.2); therefore, validating the performance of WRF by these very same observations would amount to a "self-fulfilling prophecy". Thus, not all available TAWES stations were assimilated in the WRF simulations - rather, 23 stations scattered over Austria got dropped from the assimilation scheme (hereafter referred to as "validation stations", as they serve validation purposes). For this reason, the computation of all verification metrics took place only at these validation stations (in addition to the three locations for which the FLEXPART(-WRF) simulations of greenhouse gas concentrations were conducted).

Terrain Classification of Validation Stations

As this study seeks to investigate methods of transport modelling in complex/alpine regions, a question of interest is whether ERA5 and the WRF configurations perform differently in different types of terrain (alpine/non-alpine). Therefore, for some of the verification computations, the validation stations got split into these two categories based on the following procedure.
First, the CORINE 2018 land cover dataset [Moiret-Guigand et al., 2021] was considered, which categorizes each simply connected area covering at least 25ha as a polygon patch of a certain surface type, following standardized nomenclature. In this nomenclature, the categories that come closest to describing alpine terrain are titled "bare rocks", "sparsely vegetated areas", and "glaciers and perpetual snow". Since merely considering these area types would be restrictive to mountain tops and their immediate surroundings only, this would lead to too narrow a selection. Therefore, to extend the definition of "alpine terrain" towards the understanding of simply being in the vicinity of mountains, each patch of the three mentioned land cover categories got selected and circles with a radius of 10km got drawn around them. The conjunction of all these circle areas made up the total area of Austria that was assumed to be alpine terrain as per this method. All TAWES station's coordinates were evaluated as to whether they are located in this area, and subsequently, a lookup table containing a classification of alpine/non-alpine stations was generated.
(Remark: It is obvious that the result of this table strongly depends on the selection of the classification radius. By the 10km definition of the radius, 11 of the 23 validation stations mentioned above are classified as located in alpiine terrain, and the remaining 12

as non-alpine.)

Vertical Integrity of WRF Simulations

In the process of evaluating the performance of the different WRF configurations, suspicions arose about a potentially occurring systematic error concerning wind speed with increasing altitude. To investigate this, an intercomparison between vertical profiles of horizontal wind speed of ERA5, one of the WRF configurations, and radiosonde measurements (all at the location of Vienna) was conducted.
The profiles underwent a first-sight check, and histograms of horizontal wind speeds between all the main pressure levels were compared.
According to these analyses, the possibility of a systematic error could be ruled out.
The radiosonde observations employed for this stem from the University of Wyoming Atmospheric Science Radiosonde Archive [UWyoming].

2.2.4. Verification Metrics

Throughout this study, various means of assessing the quality of results were used, such as the root mean square error (RMSE), the mean absolute error (MAE), and two types of correlations. The different methods and metrics are defined as follows.

RMSE, MAE and Correlations

Let X and T be time series of an equal amount of elements, where X is stemming from an experiment (e.g. a model) and T denotes the "truth" (e.g. according to observations).

Then, the root mean square error (RMSE) of X is defined as

$$RMSE_X = \sqrt{\frac{1}{n}\sum_{i=1}^{n}(X_i - T_i)^2}, \tag{2.9}$$

where X_i and T_i are the i-th elements of the two time series (the time series are evaluated at the same time steps), and n is the number of elements that both time series contain.

Furthermore, the mean absolute error (MAE) of X can be written as

$$MAE_X = \frac{1}{n}\sum_{i=1}^{n}|X_i - T_i|. \tag{2.10}$$

Since both these metrics increase the more X and T deviate element-wise (though the RMSE penalizes large deviations more strongly), it can be said that the smaller the resulting values, the better the quality of the time series X. Thus it becomes obvious when considering another experimental time series Y (e.g. stemming from another model), that holds that according to these two metrics, model X performs better than model Y if

$RMSE_X < RMSE_Y$ and $MAE_X < MAE_Y$, respectively.

Also, two coefficients were used to quantify how well two time series correlate. First, the Pearson correlation coefficient of a time series X with the truth T is defined as

$$\rho_X = \frac{cov(X,T)}{\sigma_X \sigma_T}, \tag{2.11}$$

where $cov(X,T)$ denotes the estimated sample covariance of X and T, and σ_X and σ_T are the sample standard deviations of the two time series.

Secondly, the Spearman correlation coefficient does not quantify correlations of the time series elements themselves but of their rank indices when ordered from least to greatest, and is defined as

$$\rho_{s_X} = \frac{cov(R[X], R[T])}{\sigma_{R[X]} \sigma_{R[T]}}, \tag{2.12}$$

where $R[X]$ and $R[T]$ represent the series of rank indices of the two time series; meaning that ρ_{s_X} describes the Pearson correlation of the two rank series.
It can be said for both the correlation coefficients that, if two experimental time series X and Y are considered, X outperforms Y with respect to these metrics if its correlation coefficients are greater than Y's.

Wind Distributions

In the assessment of quality of wind information in WRF and ERA5, comparatively to observations, histograms for wind speed, as well as for wind direction (so-called "wind roses") were computed.

The frequencies of wind speeds are statistically known to follow a Weibull distribution [Elliott et al., 2004], whose probability density function is defined as

$$f(v) = \frac{c}{s}\left(\frac{v-l}{s}\right)^{c-1} \exp\left(-\left(\frac{v-l}{s}\right)^{c}\right), \tag{2.13}$$

where v denotes the wind speed, c is a shape parameter, and l and s are horizontal shifting and scaling parameters, respectively.
Weibull distributions got fitted to observed wind speed histograms over a test period, as well as to wind speed histograms stemming from ERA5 and WRF, in order to assess which distribution's set of parameters agrees better with the one of the observations.

Taylor Diagrams

For the comparison of the capability of different models to model a certain reference spatial or temporal pattern (as e.g. provided by observational "truth"), Taylor diagrams were employed [Taylor, 2001]. A Taylor diagram visualizes the relationship of the Pearson correlation coefficient of a modelled sample and a reference, the standard deviations of these two, and the centered root mean squared difference (CRMSD) between them, in a polar plot. The computation of CRMSD is much alike the one of the RMSE, as shown in Equation (2.9), with the only difference that the sample and reference time series are expressed as deviations from their respective average values.

3. Results

3.1. Meteorological Forcing - ERA5 and WRF

With the intent of determining the suitability of FLEXPART-WRF as means of simulating atmospheric transport of greenhouse gases, it has to be investigated how accurately its input, namely WRF-modelled meteorological information, depicts the atmospheric state (see section 2.2).
The nine available WRF configurations (as seen in Table 2.2), as well as ERA5 reanalyses (which serve as meteorological input for the most conventional FLEXPART versions), were thus compared to ground observations at TAWES stations.
This comparison considered a test period of approximately 40 days (January 1 - February 9, 2022), and evaluates the most important quantities for atmospheric transport - wind (speed/direction/horizontal components), as well as temperature and pressure.
An overview of model performances for each quantity is shown below.

3.1.1. Surface Pressure

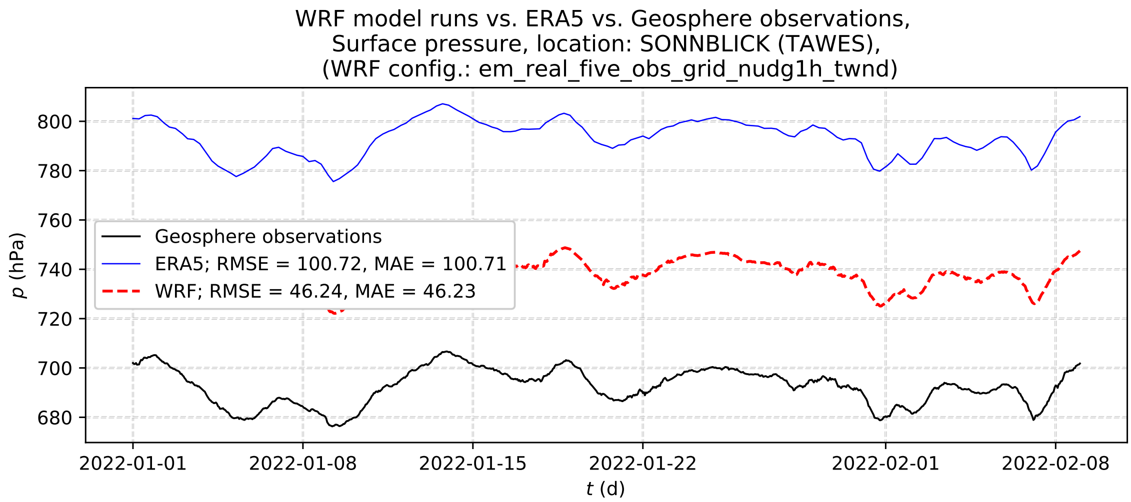

Figure 3.1.: Surface pressure; comparison of observations with ERA5 and WRF in the configuration `em_real_five_obs_grid_nudg1h_twnd`. RMSEs and MAEs in the figure legend are computed over the depicted time series and with respect to observations.

For most individual stations, as well as on average, all WRF configurations outperform ERA5 in the metrics considered (RMSE and MAE with respect to observations, as well

as correlation coeficcients). A factor playing a big role in these results is the matter of model topography - which, due to the much finer horizontal resolution of the used WRF configurations, approaches reality more closely than the topography of ERA5.
Figure 3.1 shows time series of surface pressure obtained from observations, ERA5, and one of the nine WRF configurations, at Sonnblick (one of the receptor locations for the FLEXPART/-WRF simulations), which is located at an altitude of over 3000m above sea level.

In cases of coarser model topography, peaks in orography tend to be underestimated, and valleys overestimated, respectively. Therefore at Sonnblick, being a mountaintop station, both models (WRF and ERA5) underestimate altitude (and thus overestimate surface pressure), though ERA5 does more so due to coarser resolution.
The effect of horizontal model resolution and its relation to misestimations of altitude is further depicted in the schematic Figure 3.2. (The orography profile, locations and model grid in this example are hypothetical.)

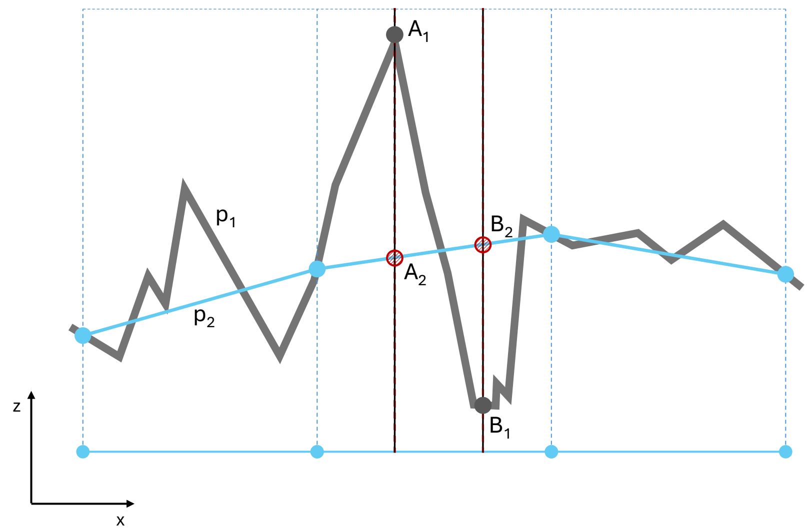

Figure 3.2.: Misestimated altitude of a mountaintop point and a valley point in a horizontally coarsely resolved geoscientific model. The thick dark grey profile represents the actual vertical cross-section of a hypothetical orography. Light blue points on the bottom horizontal line represent grid points of a geoscientific model. Intersection points of the vertical light blue dashed lines with the orography profile, and the light blue profile connecting them, depict the same orography profile, as captured by the model. Thus, the actual mountaintop point A_1, if brought to model topography, gets lowered and represented as the point A_2 in the model, with drastically decreased altitude. The opposite happens for a valley point $B1$, which, interpolated on model orography, becomes B_2, whose altitude is represented erroneously high.

Concluding, it can be said that with respect to surface pressure, the WRF configurations introduced in this project represent meteorological "truth" better than ERA5.

3.1.2. 2m Temperature

The quantity of 2m temperature exhibits more differentiated features. It becomes visible that how each model performs strongly depends on the altitude of the station. This effect can also be elucidated by the influence of the horizontal model resolution on orography (as seen in Figure 3.2), since typically, lower altitudes are associated with higher temperatures and vice versa.
More details on this can be seen in Figure 3.3, showing Taylor diagrams that classify the twenty-three validation stations (as described in Section 2.2.3) by their altitude.
While the considered metrics averaged over stations located lower than 500m a.s.l. (above sea level) display a comparable performance of ERA5 and some of the WRF configurations (such as `em_real_five_obs_grid_nudg` or `em_real_five_obs_grid_nudg1h_twnd`, etc.; see Figure 3.3a), others fall off (e.g. `em_real_no_obs_grid_nudg_Dudhia`).
Considering stations of altitude 500m $\leq z \leq$ 1000m, those WRF configurations, which lower than 500m were of approximately equal distance from observations as ERA5 (note: "distance" between observations and models in Taylor diagrams gets quantified by the CRMSD), now come closer to them than ERA5 (see Figure 3.3b), while those that were more distant from observations than ERA5 in the lowest level still remain so. The effect of ERA5 moving further away from observations than the WRF configurations increases even more when stations located higher than 1000m a.s.l. are considered (Figure 3.3c). Here, ERA5 shows a similar performance as the WRF configurations furthest from the observations.

Averaging all metrics contained in a Taylor diagram over all validation stations yields what can be seen in Figure 3.3d. Thus, it can be said that regarding 2m temperature, some WRF configurations depict observtional "reality" more accurately - particularly `em_real_five_obs_grid_nudg1h`, `em_real_five_obs_grid_nudg1h_twnd`, `em_real_five_obs_grid_nudg`, `em_real_no_obs_nudg1h` - than ERA5, and some others less (namely e.g. `em_real_no_obs_grid_nudg`, `em_real_no_obs_grid_nudg_Dudhia`, `em_real_five_obs_nudg`).

3.1.3. Wind

Quantities describing wind (u and v component; wind speed and direction, respectively) behave more ambivalently than pressure and temperature.
To summarize, it can be said that at all the release locations used for transport modelling (i.e. Vienna, Sonnblick and Innsbruck), at least some WRF configurations represent observations better than ERA5. This is unsurprising, since none of these stations is part of the validation stations that were dropped (see section 2.2.3); thus, at all of them, the observations we compare to get directly assimilated in WRF. Nonetheless, due to the importance of an accurate representation of the atmospheric state at the particle release locations for transport models, this fact is not to be dismissed.
Furthermore, it can generally be said that at a big majority of the assimilated stations, WRF improves wind directions and the representation of variability of wind speed. An

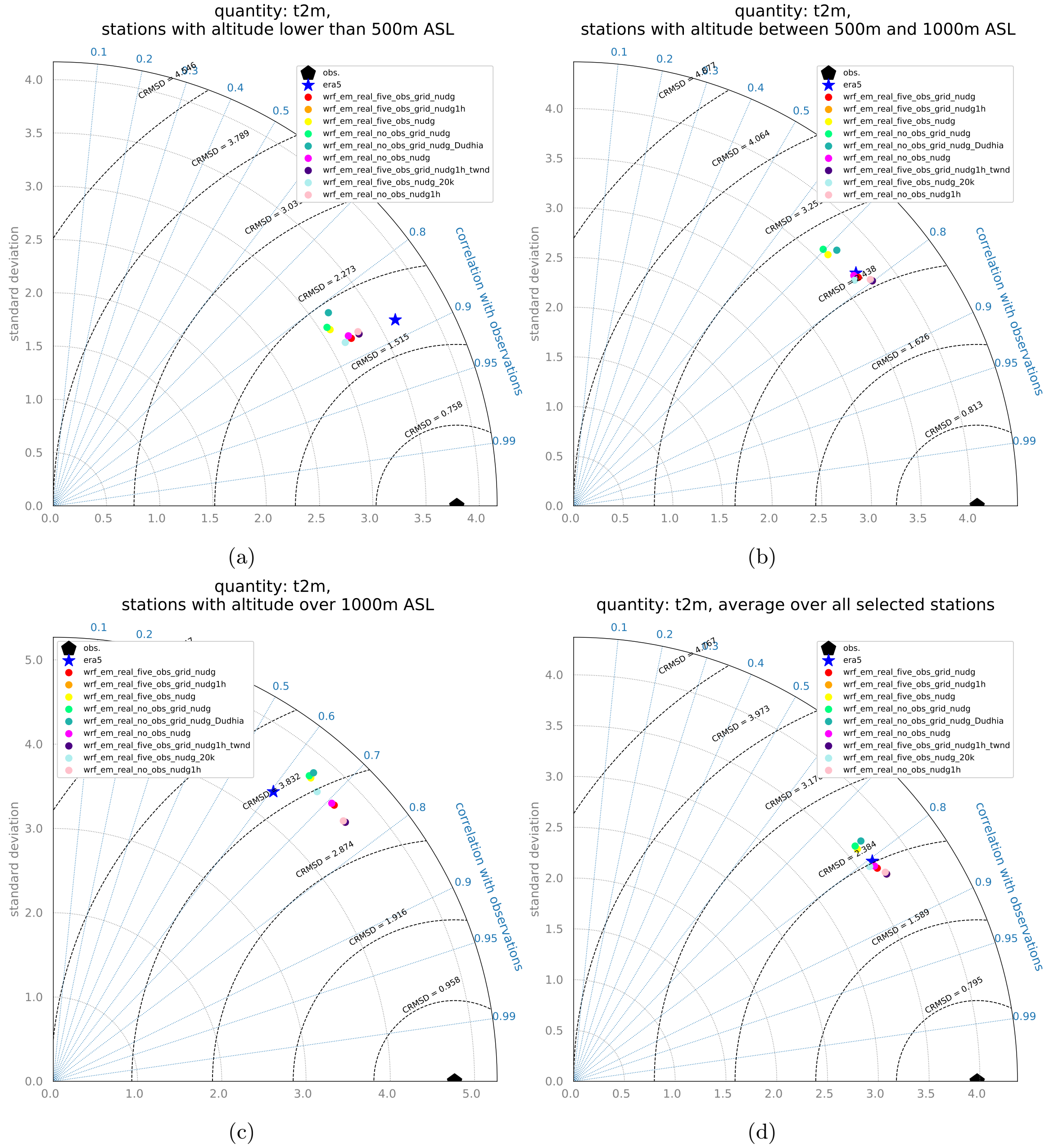

Figure 3.3.: Taylor diagrams, comparing 2m temperature standard deviations, Pearson correlations and CRMSDs with respect to observations at the twenty-three validation stations over the test period. The closer a model lies to the observational reference in terms of CRMSD, the better this model performs in regards of these metrics. (d) depicts each model's metrics when averaged over all stations, while in (a)-(c), the averaging only considers stations of increasing altitude classes. (Note: In these Taylor diagrams, as well as any other that is presented in this section, the orange dot denoting the WRF configuration `em_real_five_obs_grid_nudg1h` is invisible, as it gets entirely overshadowed by the purple one denoting `em_real_five_obs_grid_nudg1h_twnd`. In all cases and for all quantities, their metrics are almost identical.)

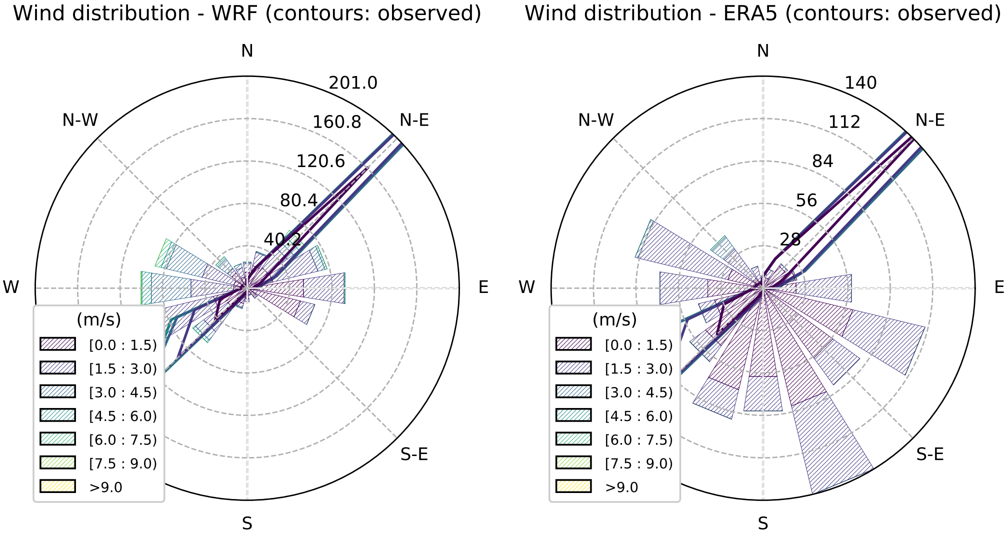

Figure 3.4.: Wind roses comparing observations with models in Langen am Arlberg throughout test period. The contours depict distributions of observed wind (directions; colors of the contours indicate wind speed intervals), while the histograms show model results (bar height representing frequency of wind direction; colored shading disaggregating to speed intervals).
Left: Observations and WRF (`em_real_five_obs_grid_nudg1h_twnd`); Right: Observations and ERA5.

example of this is shown in Figures 3.4 and 3.5, for the location of Langen am Arlberg, where the aforementioned effects take place (although the station is one of the twenty-three ones dropped from the assimilation). Figure 3.4 shows that while WRF's direction distribution is not close to the observed one, it still removes a substantial amount of wrongly estimated directions exhibited by ERA5. In Figure 3.5, it can be seen that ERA5 overestimates the frequency of low and underestimates the frequency of high wind speeds, while WRF captures the observed variability better.

Considering only the twenty-three validation stations, it can be noted the performance of WRF and ERA5 is very location-specific. There are examples of WRF clearly outperforming ERA5, and vice versa. In total, however, ERA5's capability of representing wind information in places where no observation nudging takes place slightly exceeds WRF's. An overview over this, taking into consideration different quantities (u and v component as well as wind speed), can be seen in Figure 3.6.
What is visible in Figure 3.6a is that all WRF configurations represent wind comparably well to ERA5 when only time steps from locations classified as "non-alpine" (by the definition used in section 2.2.3) are used in the comparison. Considering data stemming only from "alpine" stations, ERA5 outperforms all WRF configurations with respect to CRMSD to observations (see Figure 3.6b). This happens mainly due to WRF overestimating the variability of wind speed and its fluctuations, yielding an exaggerated standard deviation. While ERA5 underestimates it just as much, in the visualization of a Taylor diagram, overestimations get penalized more strongly. Averaging the Taylor diagram

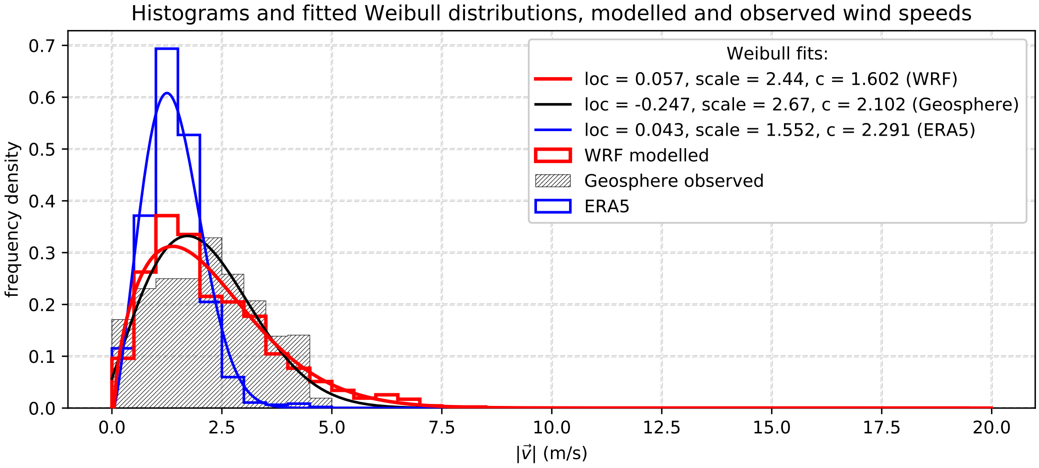

Figure 3.5.: Wind speed distributions in Langen am Arlberg throughout the test period, as recorder by observations, WRF (`em_real_five_obs_grid_nudg1h_twnd`), and ERA5. For each, a histogram and a Weibull distribution fitted to it is shown. The parameters `loc`, `scale` and `c` correspond to l, s and c as shown in Equation (2.13).

metrics of stations located at an altitude between 500m and 1000m a.s.l. (Figure 3.6c) elucidates the fact that the overestimation of variability in WRF starts in lower heights already and increases with altitude. Figure 3.6d depicts a summary of all validation stations by averaging their respective metrics.
Note: Although different quantities are used in the subfigures, it became visible in the analyses conducted for this study that the behavior of all three of them is similar.

An example for this overestimation of variability can be seen in Figure 3.7, showing wind speed absolute values throughout the test period at the station Rinn (one of the validation stations; located in mountainous surroundings).

In light of these results, to rule out the possibility of a systematic error of wind overestimation in high altitudes in WRF, a comparison of wind speed frequency distributions between ERA5, WRF and radiosonde observations at Wien Hohe Warte for different altitude levels got conducted (see Appendix, A.1). According to this analysis, the possibility of the exaggerated variability in WRF being caused by such an error can be excluded.

Out of all nine WRF configurations, similarly to 2m temperature (as described above), the best-performing ones again show to be `em_real_five_obs_grid_nudg1h` and `em_real_five_obs_grid_nudg1h_twnd`, followed by `em_real_five_obs_grid_nudg` and `em_real_no_obs_nudg1h`.

3.2. Greenhouse Gas Concentration Simulations

After investigating how well ERA5 and WRF are suited to supply meteorological forcing for atmospheric transport models in an Austrian domain, the following section

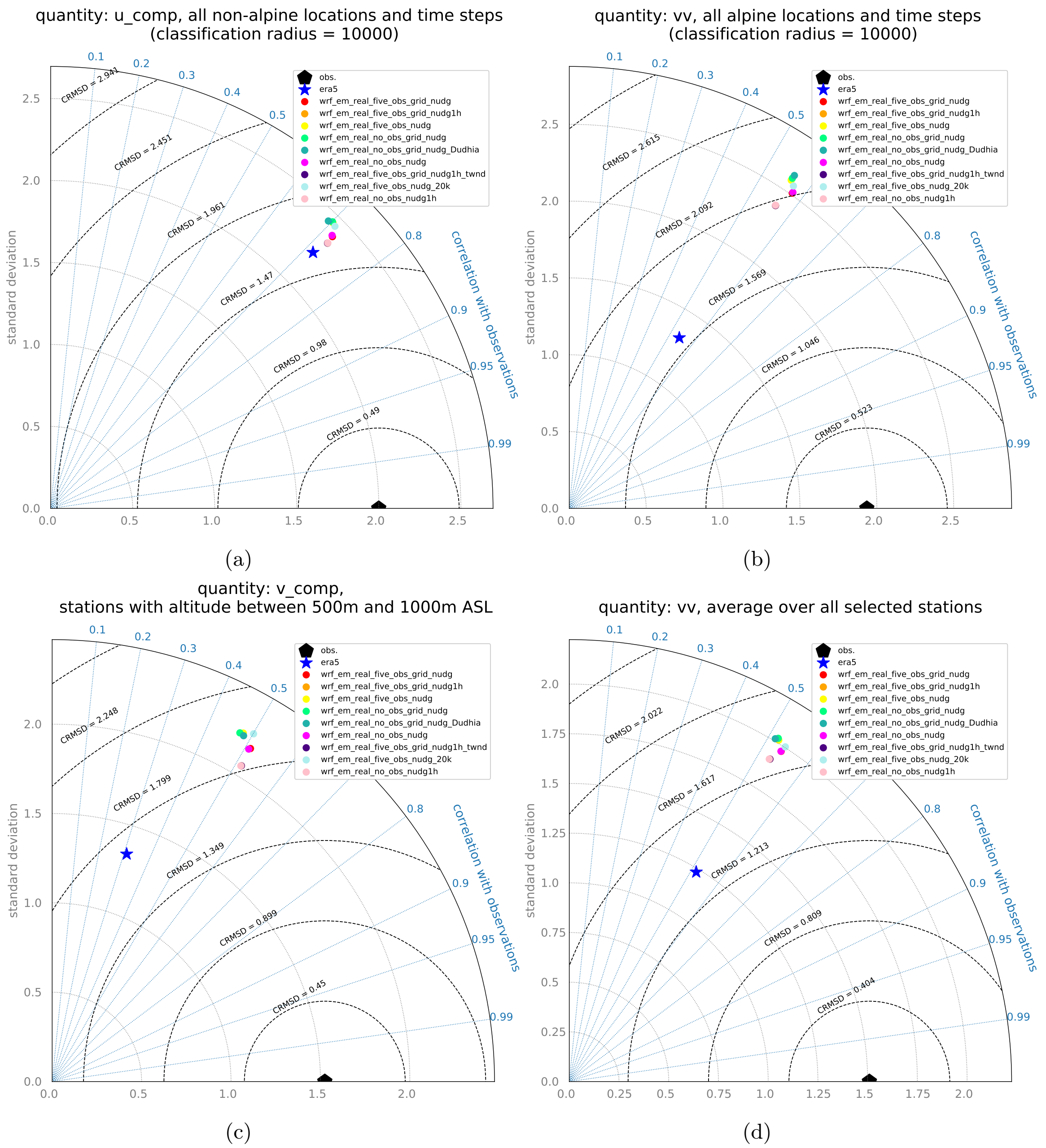

Figure 3.6.: Taylor diagrams of: (a) the u wind component, computed over all locations and time steps of stations situated in non-alpine terrain; (b) wind speed, computed over all locations and time steps of stations in alpine terrain; (c) v wind component, metrics averaged over all stations with altitude between 550m and 1000m a.s.l.; (d) wind speed, metrics averaged over all twenty-three validation stations.

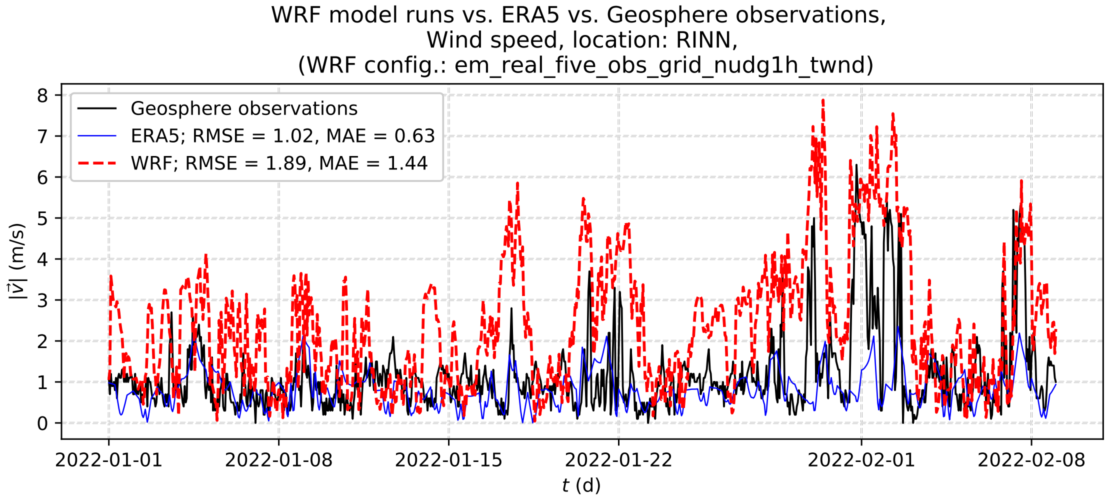

Figure 3.7.: Time series of wind speed at the station Rinn (observations, ERA5, and WRF configuration `em_real_five_obs_grid_nudg1h_twnd`).

compares greenhouse gas concentrations modelled by FLEXPART-WRF (input from the `em_real_five_obs_grid_nudg1h_twnd` configuration) and FLEXPART-ECMWF, as well as observations.

This is done for CH_4 and CO_2, at all Austrian stations supplying concentration measurements of these species - Universität Innsbruck, Sonnblick observatory, and Vienna (Arsenal tower), for a simulation period of the year 2022. Before presenting the results of this, there follows a description of experiments assessing the loss of initial condition sensitivity in FLEXPART-WRF (see Section 2.1.5), as well as the efficacy in mitigating the issue by using a version of the model incorporating the corrective steps proposed above.

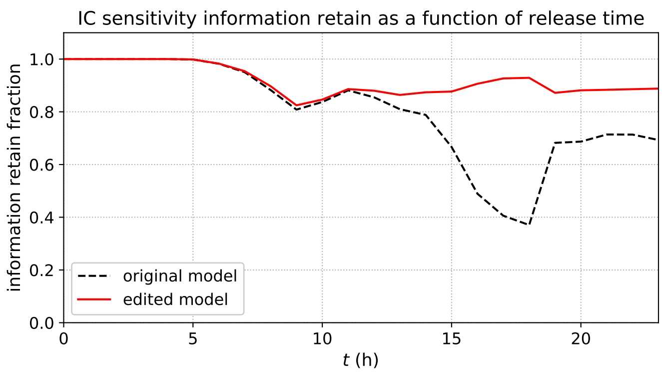

Figure 3.8.: First experiment on IS information retain of a 24h FLEXPART-WRF backward simulation on Austrian domain, getting cut at the start of that simulation period (i.e. each time step shows backward travel time of its release).

3.2.1. Initial Condition Sensitivity in FLEXPART-WRF

Section 2.1.5 describes how in FLEXPART-WRF, when using a non-global domain, there occurs a systematic error of particles not getting terminated on time when leaving the simulation domain.

In this study, two experiments were conducted with two different versions of FLEXPART-WRF - the original one, and one implementing the treatment of this issue as described in 2.1.5. The underlying idea of both these experiments is computing a generic backward simulation (with a domain covering Austria; as all FLEXPART-WRF simulations in this project; see Fig. 2.2), covering a time period of one day, with hourly temporal resolution (not only is the output resolution hourly, but moreover, each hour of the day, a particle release is taking place). Each of these 24 releases therefore is associated with its individual initial condition sensitivity field, denoted by IS in Equation (2.8) (which in a full concentration simulation serves for multiplying it with background concentrations of the modelled species), which, in a properly working model framework must all individually sum up to 1. However, with particles erroneously leaving the domain, some fraction of this initial sensitivity information gets lost.

Figure 3.8 depicts the results of the first experiment. In this scenario, the backward simulation got cut off at the beginning of the one-day simulation period; meaning, the particles released at time step one had only one hour to be transported, those of the release at time step two travelled two hours back in time, etc. It can be seen, then, that while for a few hours of particles travelling, the corrected and original version of the model retain the complete amount of initial sensitivity information, but subsequently, different fractions of every release's particles leave the domain. This fraction, in the original model, is expected to increase monotonically (except for random fluctuations due to the specific meteorological conditions; which for such short simulation times show to be substantial), leaving as little as 40% of information in the domain (for particles having only travelled e.g. 18 hours); whereas in the corrected model (before normalizing), the retained information ratio remains somewhat consistently above 80%. (Note: As mentioned above, the reason for the information retain still amounting to sub-100% is currently unclear. However, as the two experiments show, the fluctuations seem random and exhibit no decaying trend.)

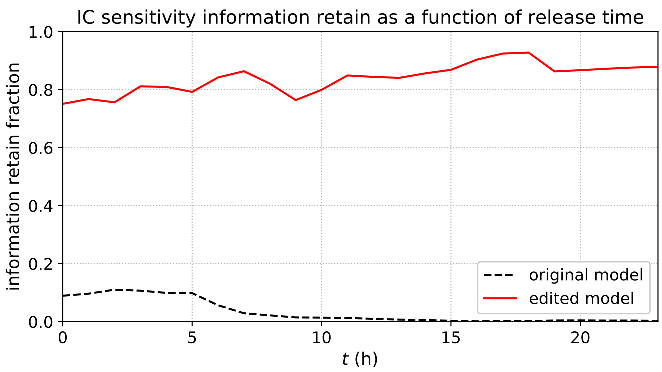

Figure 3.9.: Second experiment on IS information retain of a 24h FLEXPART-WRF backward simulation on Austrian domain. This time, the simulation extends to 48h prior to the start of the simulation period (i.e. for each time t, particles released then are traced back t + 48h).

The second experiment, shown in Figure 3.9, does not cut off the backward simulation at the beginning of the 24-hour simulation period, but traces back the particles for another 48 hours beyond that (which is the backward simulation time chosen for the actual FLEXPART-WRF simulations in this study). Thus, the release of the zero time

step has travelled for a total of 48h and the last one for three full days. In this case, for the original model, at best about 10% of initial sensitivity information remains, while the value approaches zero on any occasion where particles need to be followed for longer than 2.5 days on such a limited domain. However, the corrected version of the model consistently displays values between 75 and over 90%, before normalizing.
(Remark: Although the aforementioned need for normalization of the initial sensitivity fields to 1 - see Section 2.1.5 - persists even in the corrected model, it would not be possible to circumvent the issue of information loss by merely normalizing the fields obtained from the original model. This is due to the fact that on a spatially limited domain like the one of this study, initial sensitivity fields frequently are zero everywhere even after simulation times of less than three days, therefore not allowing for any normalization. In contrast, the corrected model's steadily high levels - between 75% and 100% - of information retain provide enough "susbtance" for normalizing them to 1.)

3.2.2. CH_4

In this section, modelling results of CH_4 concentration time series are presented. Figure 3.10 depicts observed time series of CH_4, and concentrations modelled by FLEXPART-WRF and FLEXPART-ECMWF, at the three simulation locations. Since these respective time series have different temporal resolutions (e.g. FLEXPART-WRF simulations: hourly, FLEXPART-ECMWF: three-hourly), the only time steps considered in these figures are the ones common to all of them. To illustrate: The late start and data gap in the Vienna time series happens due to a lack of observation availability. Respectively, there are no FLEXPART-ECMWF simulations available for the first ten days of January, since FLEXPART-ECMWF's backward simulation time is ten days. The figure also displays the RMSE and MAE metrics, as defined in Section 2.2.4, for each receptor site.

In Figure 3.11, the left-hand side column contains scatterplots (including correlation coefficients) of CH_4 for the three sites. For the data points of the scatterplots, again, only time steps at which all three data sources (observations, FLEXPART-WRF and FLEXPART-ECMWF simulations) are available could be considered.
The right-hand side column shows concentration frequency distributions (as well as their mean values over the whole simulation period) for the three locations.

3.2.3. CO_2

Analogously to CH_4 , the same set of figures follows for CO_2. Figure 3.12 contains time series from all three data sources (observed, FLEXPART-WRF-modelled, FLEXPART-ECMWF-modelled) for all three simulation locations (Innsbruck, Sonnblick, Vienna), according to the overlap of their availability. Figure 3.13, again, shows scatterplots (including Pearson and Spearman correlation coefficients) in its left-hand side column; as well as concentration frequency distributions and their mean values over the simulation period on the right-hand side.

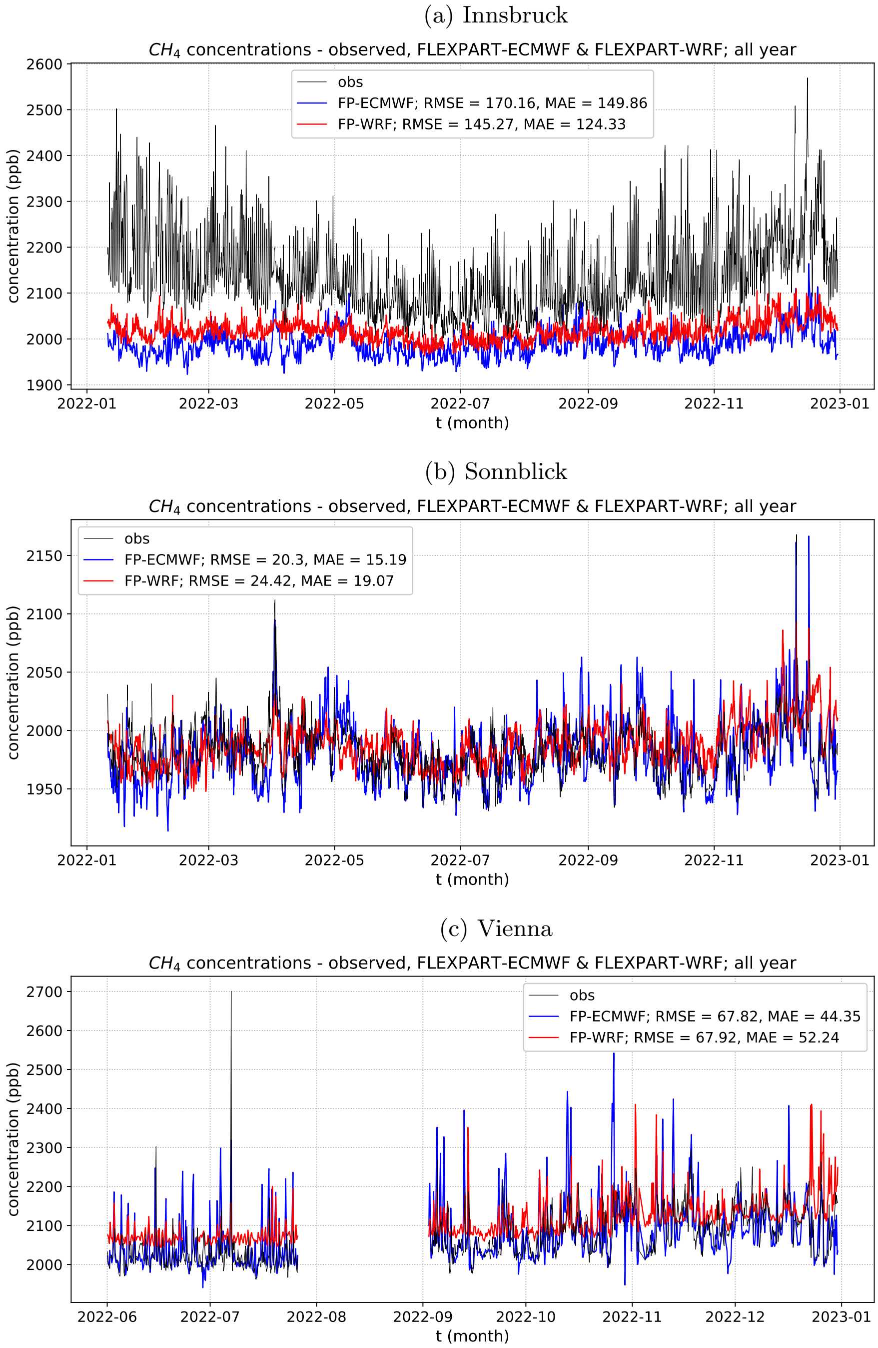

Figure 3.10.: Time series of observed, FLEXPART-WRF-modelled, and FLEXPART-ECMWF-modelled CH_4 concentrations, at Innsbruck, Sonnblick and Vienna - Arsenal tower. RMSE and MAE with respect to observations.

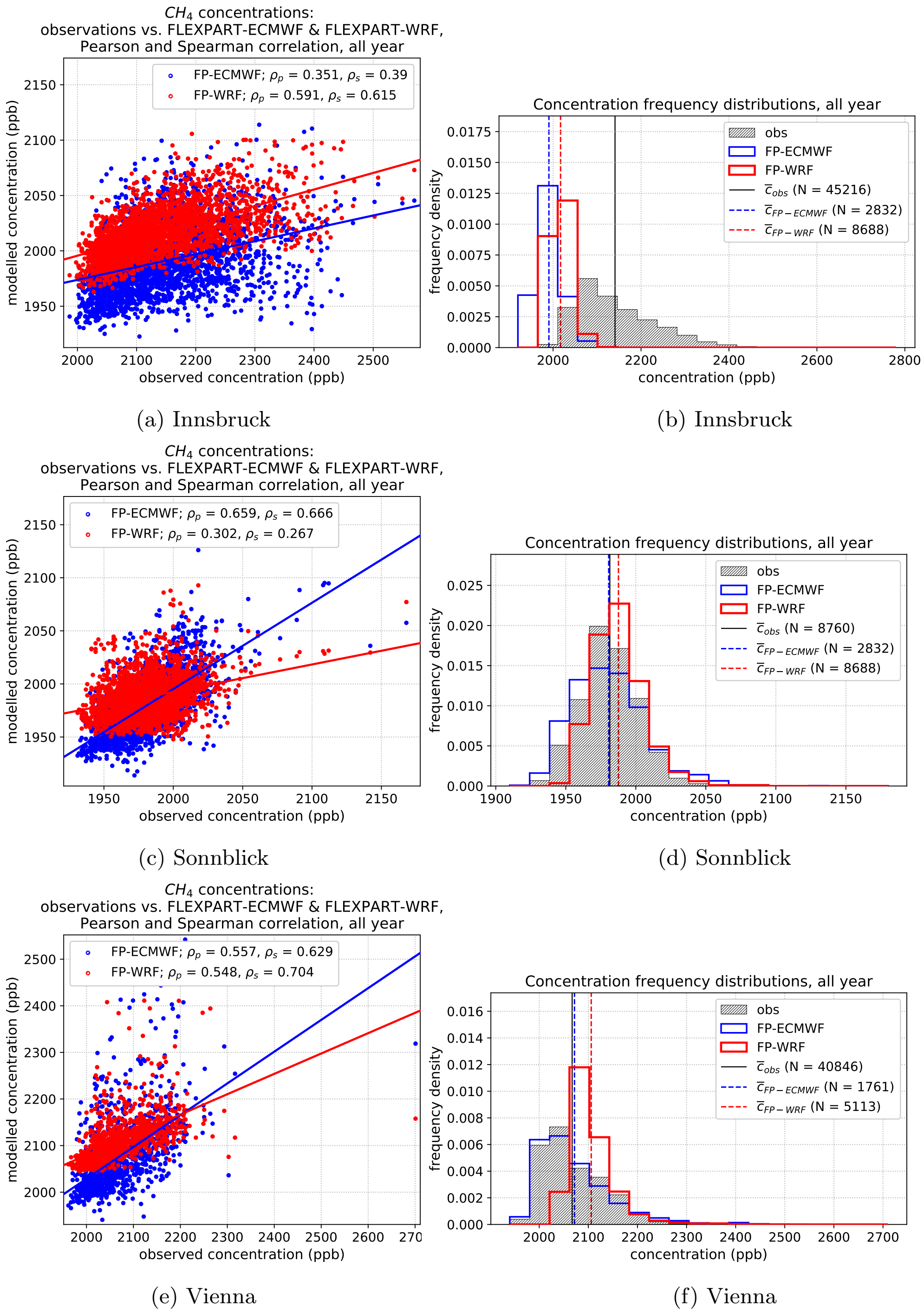

(a) Innsbruck (b) Innsbruck

(c) Sonnblick (d) Sonnblick

(e) Vienna (f) Vienna

Figure 3.11.: Left: Scatterplots of CH_4 concentrations as observed vs. results of the two models. ρ_p and ρ_s denote Pearson and Spearman correlation coefficients. Right: Histograms of observed, FLEXPART-WRF and FLEXPART-ECMWF CH_4 concentration values at all available time steps. The vertical lines display mean values of the three distributions.

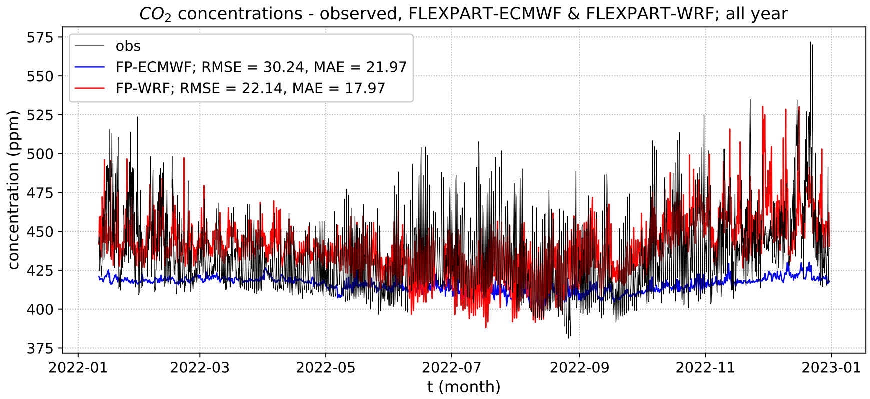

(a) Innsbruck

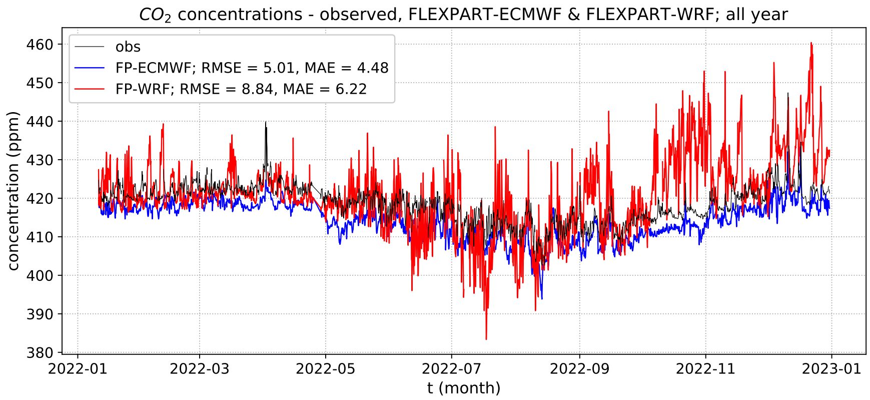

(b) Sonnblick

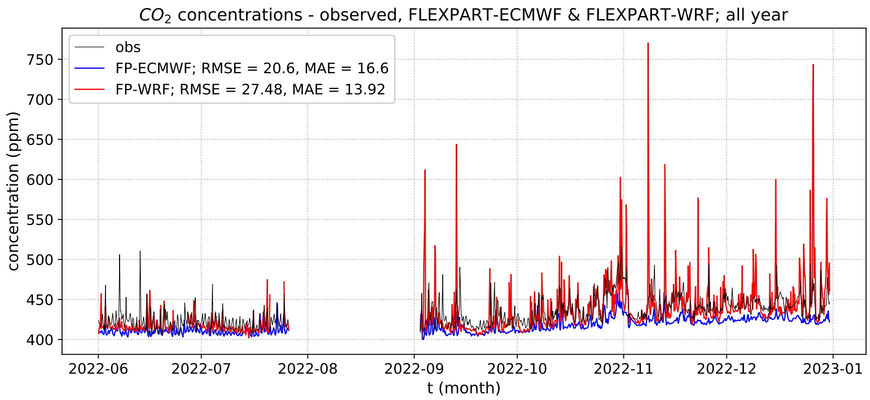

(c) Vienna

Figure 3.12.: Time series of CO_2 concentrations in Innsbruck, Sonnblick and Vienna, stemming from observations, FLEXPART-WRF, and FLEXPART-ECMWF simulations. RMSE and MAE metrics for model time series are with respect to observations.

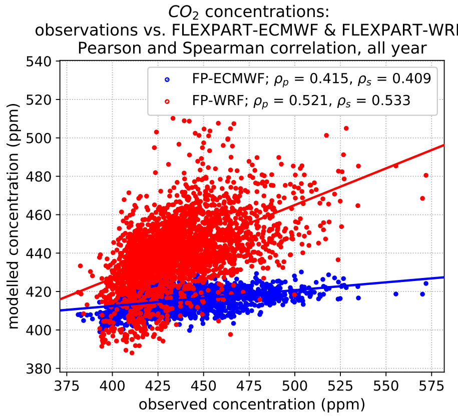

(a) Innsbruck

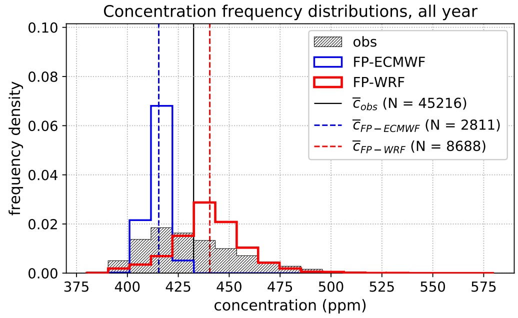

(b) Innsbruck

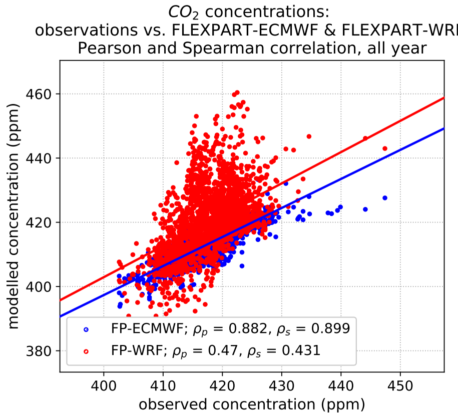

(c) Sonnblick

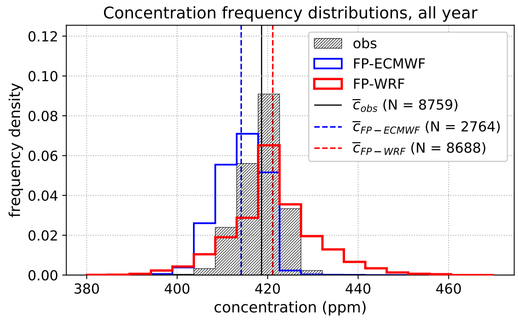

(d) Sonnblick

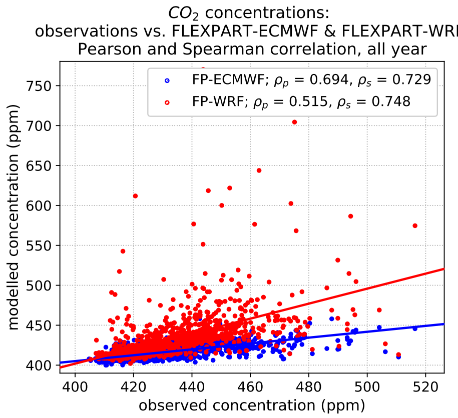

(e) Vienna

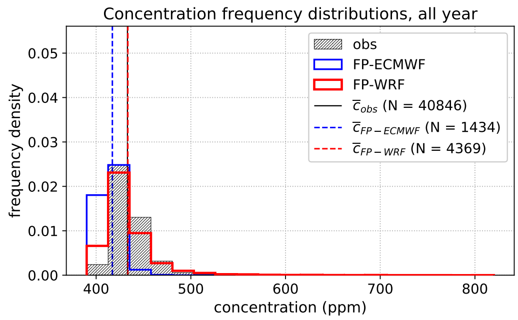

(f) Vienna

Figure 3.13.: Left: CO_2 concentration scatterplots with Pearson and Spearman correlations (ρ_p, ρ_s), observed vs. modelled by the two models. Right: Histograms of CO_2 concentration frequency distributions, including their mean values (represented by vertical lines).

4. Discussion

Regarding the representation of meteorological information by ERA5 and WRF for the input/forcing of atmospheric transport models, it can be said that the use of WRF has several advantages.
First and foremost, there is the matter of spatial (and temporal) resolution, on which WRF offers considerable flexibility (whereas with ERA5, desired resolutions can only be obtained by interpolating). This is particularly crucial when focusing on areas of more complex terrain, as those that are dealt with in this study.
With regard to WRF's capabilities of representing atmospheric state variables that are important for atmospheric transport modelling, there are different factors to take into account. It is clear that WRF (mainly due to resolution) better represents quantities like surface pressure and temperature (see Figures 3.1, 3.2, 3.3). As seen in these figures, for temperature, the choice of WRF configuration is more delicate than for pressure. The configurations representing 2m temperature best are those incorporating hourly grid and observation nudging (`em_real_five_obs_grid_nudg1h` and `em_real_five_obs_grid_nudg1h_twnd`), closely followed by `em_real_no_obs_nudg1h`, which employs hourly grid nudging only (no observation nudging). Another set of configurations still outperforming ERA5 with respect to 2m temperature (although less accurate than the three previously mentioned) consists of those using grid nudging every three hours, namely, `em_real_five_obs_grid_nudg` and `em_real_no_obs_nudg` (with the former, also including observation nudging, showing better results). Showing the least accuracy are the configurations using neither observation- nor grid nudging (`em_real_no_obs_grid_nudg`, `em_real_no_obs_grid_nudg_Dudhia`), followed by `em_real_five_obs_nudg`, which incorporates observation nudging only. When solely using observation nudging, it can be seen that the simulation quality with respect to 2m temperature can be increased by increasing the nudging radius. `em_real_five_obs_nudg_20k`, employing a nudging radius of 20km, even performs comparably to ERA5 on average (Figure 3.3d), unlike `em_real_five_obs_nudg` (with observation nudging within a 5km radius).
To summarize, it can be said that WRF's advantage over ERA5 of improved horizontal resolution, combined with hourly grid nudging towards ERA5, suffices to achieve a more accurate 2m temperature representation than with ERA5. While these constitute the most important aspects of WRF's performance exceeding ERA5's, further improvement can be brought by additional observation nudging. Furthermore, it becomes clear that despite the advantage in horizontal model resolution, WRF with observation nudging on its own, in absence of grid nudging, cannot outperform ERA5.
While the extra dependencies of WRF (on grid and observation nudging) can be interpreted as a drawback, the flexibility offered by WRF concerning the assimilation of data from specific sources can also be effectively harnessed - as an example: in a regional study

like this, the ability to customize the weights that specific observations, such as those from the TAWES network utilized here, may be desired.
The most ambivalent picture is seen in all quantities that are related to wind. As shown in Figures 3.4, 3.5 and 3.6, WRF exceeds ERA5's capabilites of capturing wind speed variability, and also shows strongly improved wind direction distributions for many locations. However, WRF displays a few drawbacks, as well. First, its performance in wind representation depends on observation coverage available for nudging - as visible by the fact that the WRF configurations that are falling behind the most are the ones lacking observational nudging (`em_real_no_obs_grid_nudg` and `em_real_no_obs_grid_nudg_Dudhia`). Second, WRF in this study shows a tendency of overestimating wind speeds at stations of higher altitude or in more complex terrain (in some caseses severely; see Figure 3.7. Considering these points, it can be said that ERA5, under some circumstances, represents wind information more accurately than WRF. Generally, it can be said that for the performance of the different WRF configurations, the same principles as for 2m temperature (described above) apply. The most accurately performing configurations prove to be those incorporating hourly grid and observation nudging, namely, `em_real_five_obs_grid_nudg1h` and `em_real_five_obs_grid_nudg1h_twnd`.

To summarize, while WRF exhibits the mentioned drawbacks, one can nonetheless profit from its flexibility in regards to resolution and data assimilation, when employing it as meteorological forcing for atmospheric transport modelling. According to the above analysis of the performance of the different configurations at representing the atmospheric state, the `em_real_five_obs_grid_nudg1h_twnd` simulations got chosen to serve as input for the FLEXPART-WRF model computations.

The issues with the implementation of the initial condition sensitivity computation in FLEXPART-WRF have been resolved sufficiently for the purposes of this study (Sections 2.1.5 and 3.2.1). While the solution is far from rigorous and not yielding an information retain of 100% (see Figures 3.8 and 3.9), combining it with a normalization of initial sensitivity fields to 1 showed successful. Please note, however, that this edit to the model got applied to FLEXPART-WRF only for output grids defined in degrees of longitude/latitude.
Future research is encouraged to extend the approach of this study towards all possible input and output grid options of FLEXPART-WRF, as well as provide a more general treatment of the initial sensitivity issue on non-global simulation domains.

As for the main goal of this study, namely, investigating whether a FLEXPART-WRF setup as used here is able to handle challenges of atmospheric transport modelling in alpine terrain like Austria (at the example of greenhouse gas concentration simulations) better than more conventional FLEXPART-ECMWF approaches, the findings are shown below.
First, it can be noted that at a site like the Sonnblick observatory, although located in alpine terrain (at a mountain peak over 3000m a.s.l.), FLEXPART-ECMWF clearly reproduces measured concentration time series of both CH_4 and CO_2 better than FLEXPART-WRF

(see Figures 3.10b, 3.11c, 3.11d, 3.12b, 3.13c, 3.13d). This owes to the fact that the main mechanism of atmospheric transport influencing concentrations of these species at a mountaintop location like Sonnblick is long-range transport due to synoptic phenomena, whose representation is one of ERA5's core qualities. One of FLEXPART-ECMWF's shortcomings, the smoothing of topography caused by coarse resolution of the ERA5 reanalyses, can be counteracted by setting the FLEXPART particle release height to the actual altitude above sea level of the Sonnblick observatory (instead of using the model ground level as reference).

Looking at Innsbruck's CH_4 and CO_2 concentrations, however, the picture is entirely different. Although this station is located in alpine terrain as well (in the Inn valley), FLEXPART-WRF's morelled results lie much closer to observed concentrations according to every used metric without exceptions. While in regard to CH_4 both models lack variability that is contained in the observations, FLEXPART-WRF is able to reduce RMSE and MAE from what is obtained by FLEXPART-ECMWF (3.10a). Furthermore, FLEXPART-WRF exceeds FLEXPART-ECMWF's correlation with observations (Figure 3.11a), and its average concentration value over the whole simulation period lies closer to the observed one than the one of FLEXPART-ECMWF. For CO_2 in Innsbruck, the appearance is similar (although FLEXPART-WRF here does capture the temporal variability seen in the observations much better than FLEXPART-ECMWF; see Figure 3.12a). Again, FLEXPART-WRF produces better correlations, mean concentration value and frequency distribution than FLEXPART-ECMWF (Figures 3.13a, 3.13b).

Viewing the results for CH_4 in Vienna, it shows the RMSEs of the two models to be almost identical (FLEXPART-WRF's is larger by 0.1ppb), however, FLEXPART-ECMWF's MAE is far smaller than FLEXPART-WRF's (see Figure 3.10c). As mentioned in Section 2.2.4, the RMSE penalizes outliers stronger than the MAE, whereas the MAE is more sensitive to a large quantity of smaller deviations (which is the situation here) than to, say, a handful of outliers. The main shortcoming of FLEXPART-WRF here seems to be a lack of variability, and a slightly overestimated baseline. Pearson correlations are also almost identical (FLEXPART-ECMWF exceeds FLEXPART-WRF by less than 1% only); however, FLEXPART-WRF exhibits a much higher Spearman correlation (Figure 3.11e). In terms of all-year means, FLEXPART-ECMWF comes very close to observations, while FLEXPART-WRF clearly overestimates it (due to aforementioned exaggerated baseline; Figure 3.11f). There are some similarities to the CH_4 concentrations in the case of CO_2 in Vienna; again, the metrics obtained are mixed. However, here the situation is in a sense the other way around: FLEXPART-ECMWF's RMSE is clearly lower than FLEXPART-WRF's, but the reverse is true for the MAE (Figure 3.12c). This is happening since the main drawback of FLEXPART-WRF here is not a shifted baseline concentration, but a number of extreme-value events (outliers), which get penalized much more strongly by the RMSE. The issue of outliers is also central to correlations (Figure 3.13e). While the Pearson correlation coefficient is very outlier-sensitive (thus, FLEXPART-ECMWF outperforms FLEXPART-WRF with respect to it), the Spearman correlation shows to be more robust in such a situation, due to its computation from ranks of the values (which causes FLEXPART-WRF's to exceed FLEXPART-ECMWF's). Furthermore, aside from the outliers, FLEXPART-WRF clearly represents the variability of CO_2 concentrations better than FLEXPART, and even yields a mean concentration value almost identical to the one of the observations (see Figure 3.13f).

To sum it up, it can be said that FLEXPART-ECMWF clearly performs better in reproducing greenhouse gas concentrations at mountaintop locations, such as Sonnblick. In the mountaineous valley area, in which Innsbruck is situated, FLEXPART-WRF's representation of greenhouse gas concentrations is unequivocally better than FLEXPART-ECMWF's. While results are mixed for CH_4 in Vienna, for CO_2, all metrics would clearly be in favor of FLEXPART-WRF, if it was not for a handful of extreme values, and even in spite of them, FLEXPART-WRF certainly does not perform worse.

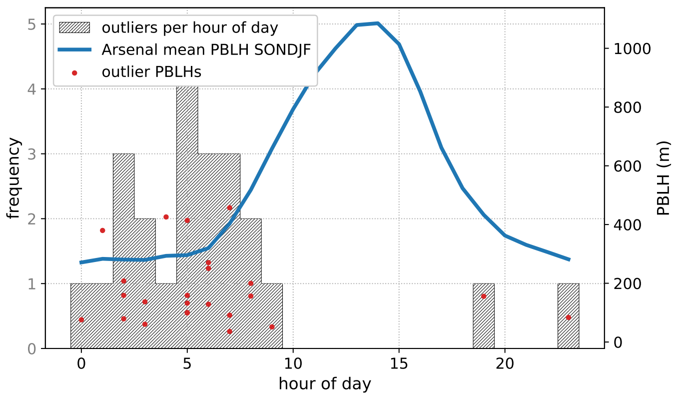

Figure 4.1.: FLEXPART-WRF Vienna CO_2 concentration simulation outlier distribution over the hours of the day, and expected planetary boundary layer (PBL) height as a function of hour of the day.
Light grey histogram: Outlier frequency over hour of day. Red dots: PBL heights at times of each of the 24 outliers, also over hour of day. Blue curve: Expected autumn/winter PBL height at each hour of day at Vienna Arsenal tower (computed as September-December and January-February average of WRF-modelled PBL heights).

Further analysis allowed to gain some insight on the nature and occurence of these outliers in the FLEXPART-WRF-modelled CO_2 concentrations of Vienna. Figure 4.1 contains information about 24 values/time steps (scattered from September to December; autumn/winter) in Vienna's CO_2 concentration time series that got classified as outliers (the threshold was arbitrarily chosen as 600ppm). Considering the time stamps of these 24 values, it became apparent that it is not uncommon for a few of these values at once to be associated with the same peak; i.e., there are far less than 24 (namely, seven) of these extreme events. The histogram of outlier frequency shows that the bulk of outliers happens during night time. Furthermore, considering the planetary boundary layer heights (PBLHs) associated with these 24 concentration values, it gets visible that in 20/24 extreme value cases, PBLH was lower than what would be expected, as indicated by the blue curve (which depicts the WRF average autumn/winter PBLH at Arsenal tower, as a function of the hour of day).

Moreover, viewing time series of each emission component contributing to the total concentration, it became evident that in all cases, with zero exceptions, the anthropogenic emission component causes the outliers. What certainly plays a part in this is that the particle release location, Arsenal tower in Vienna, is situated almost exactly on the boundary of two different grid cells of the anthropogenic CO_2 emission inventory - one of

them displaying consistently low emissions, and the other one representing the majority of anthropogenic CO_2 emissions of the whole city of Vienna (see example in A.2).
In light of these insights, it can be summarized that outliers in the Vienna CO_2 concentrations are commonly associated with PBLHs lower than expected, as well as with unfortunate geometry in the anthropogenic emission inventory. Likely, if it was not for a possible underestimation of the PBLH of WRF (e.g. due to city heat fluxes that are unaccounted for, such as traffic or domestic heating etc.), as well as the coarse resolution of the emission inventory (and the grid cell boundary coincidentally crossing the particle release location), results would be significantly improved.

In conclusion, while the handling of complex terrain and smaller-scale phenomena of the FLEXPART-WRF setup in this project in Innsbruck looks promising, there is room for further research and improvement in order for it to be used for, e.g., a full inverse modelling framework. For one, the implementation of initial sensitivity computation in FLEXPART-WRF on limited domains, as introduced in this study, must be generalized and carried out rigorously. Additionally, improving resolutions of emission inventories is crucial for obtaining more realistic greenhouse gas concentrations from the model. Nonetheless, utilizing WRF's flexibility in terms of model resolution and general customizability bears potential for atmospheric transport modelling endeavors that is not to be underestimated.

Bibliography

Dan Archer, Michael Eby, Victor Brovkin, Andy Ridgwell, Long Cao, Uwe Mikolajewicz, Ken Caldeira, Katsumi Matsumoto, Guy Munhoven, Alvaro Montenegro, and Kathy Tokos. Atmospheric lifetime of fossil fuel carbon dioxide. *Annual Review of Earth and Planetary Sciences, v.37, 117-134 (2009)*, 37, 05 2009. doi: 10.1146/annurev.earth.031208.100206.

Katharina Baier, M. Duetsch, M. Mayer, Lucie Bakels, L. Haimberger, and A. Stohl. The role of atmospheric transport for el niño-southern oscillation teleconnections. *Geophysical Research Letters*, 49, 12 2022. doi: 10.1029/2022GL100906.

Lucie Bakels, Daria Tatsii, Anne Tipka, Rona Thompson, Marina Dütsch, Michael Blaschek, Petra Seibert, Katharina Baier, Silvia Bucci, Massimo Cassiani, Sabine Eckhardt, Christine Groot Zwaaftink, Stephan Henne, Pirmin Kaufmann, Vincent Lechner, Christian Maurer, Marie Daniëlle Mulder, Ignacio Pisso, Andreas Plach, and Andreas Stohl. Flexpart version 11: improved accuracy, efficiency, and flexibility. *Geoscientific Model Development*, 17:7595–7627, 10 2024. doi: 10.5194/gmd-17-7595-2024.

Peter Bergamaschi, Ana Danila, Ray Weiss, P. Ciais, R. Thompson, Dominik Brunner, Ingeborg Levin, Y. Meijer, Frederic Chevallier, G. Janssens-Maenhout, H. Bovensmann, D. Crisp, S. Basu, E. Dlugokencky, Richard Engelen, Christoph Gerbig, Dirk Günther, Samuel Hammer, Stephan Henne, and Maarten Krol. *Atmospheric monitoring and inverse modelling for verification of greenhouse gas inventories.* 08 2018. ISBN 978-92-79-88938-7. doi: 10.2760/759928.

Peter Bergamaschi, A.J. Segers, Dominik Brunner, Jean-Matthieu Haussaire, Stephan Henne, Michel Ramonet, Tim Arnold, Tobias Biermann, Huilin Chen, Sébastien Conil, Marc Delmotte, Grant Forster, Arnoud Frumau, Dagmar Kubistin, Xin Lan, Markus Leuenberger, Matthias Lindauer, M. Lopez, Giovanni Manca, and Camille Yver. High-resolution inverse modelling of european ch4 emissions using the novel flexpart-cosmo tm5 4dvar inverse modelling system. *Atmospheric Chemistry and Physics*, 22:13243–13268, 10 2022. doi: 10.5194/acp-22-13243-2022.

A.A. Bloom, K.W. Bowman, M. Lee, A.J. Turner, R. Schroeder, J.R. Worden, R.J. Weidner, K.C. McDonald, and D.J. Jacob. Cms: Global 0.5-deg wetland methane emissions and uncertainty (wetcharts v1.3.1), 2021. URL `https://daac.ornl.gov/cgi-bin/dsviewer.pl?ds_id=1915`.

J. Brioude, W Angevine, Stuart McKeen, and E.-Y Hsie. Numerical uncertainty at mesoscale in a lagrangian model in complex terrain. *Geoscientific Model Development*, 5:1127–1136, 09 2012. doi: 10.5194/gmd-5-1127-2012.

J. Brioude, Delia Arnold Arias, Andreas Stohl, Massimo Cassiani, Don Morton, P. Seibert, W. Angevine, Stephanie Evan, Adam Dingwell, J. Fast, R. Easter, Ignacio Pisso, John Burkhart, and Gerhard Wotawa. The lagrangian particle dispersion model flexpart-wrf version 3.1. *Geoscientific Model Development*, 6:1889–1904, 11 2013. doi: 10.5194/gmd-6-1889-2013.

Silvia Bucci, Camille Richon, and Lucie Bakels. Exploring the transport path of oceanic microplastics in the atmosphere. *Environmental science & technology*, 58, 07 2024. doi: 10.1021/acs.est.4c03216.

CAMS-ANT-GLOB. Copernicus atmosphere monitoring service (2022): Cams global biomass burning emissions based on fire radiative power (gfas). `https://eccad.sedoo.fr/#/metadata/479`.

CAMS-ANT-REG. `https://eccad.sedoo.fr/#/metadata/608`.

CAMS-GFAS. Copernicus atmosphere monitoring service (2022): Cams global biomass burning emissions based on fire radiative power (gfas). `https://ads.atmosphere.copernicus.eu/datasets/cams-global-fire-emissions-gfas?tab=overview`.

CarboScope. `https://www.bgc-jena.mpg.de/CarboScope/?ID=oc_v2024E`.

Petra Dolšak Lavrič, Andreja Kukec, and Rahela Žabkar. State of the art emission inventory and their application: Literature review. *Sanitarno inženirstvo International Journal of Sanitary Engineering Research*, 15:31–46, 10 2023. doi: 10.2478/ijser-2022-0004.

Dennis Elliott, Marc Schwartz, and George Scott. Wind resource base. In Cutler J. Cleveland, editor, *Encyclopedia of Energy*, pages 465–479. Elsevier, New York, 2004. ISBN 978-0-12-176480-7. doi: https://doi.org/10.1016/B0-12-176480-X/00335-1. URL `https://www.sciencedirect.com/science/article/pii/B012176480X003351`.

EPA. `https://www.epa.gov/report-environment/greenhouse-gases#:~:text=Carbon%20dioxide%20is%20widely%20reported,warming%20associated%20with%20human%20activities.`

G. Etiope, G. Ciotoli, S. Schwietzke, and M. Schoell. Gridded maps of geological methane emissions and their isotopic signature. *Earth System Science Data*, 11(1):1–22, 2019. doi: 10.5194/essd-11-1-2019. URL `https://essd.copernicus.org/articles/11/1/2019/`.

Jerome Fast and Richard Easter. A lagrangian particle dispersion model compatible with wrf. 01 2006.

GeoSphere. https://data.hub.geosphere.at/dataset/synop-v1-1h.

GeoSphere2. https://data.hub.geosphere.at/dataset/klima-v1-1h.

T. Glauch, J. Marshall, C. Gerbig, S. Botía, M. Gałkowski, S. N. Vardag, and A. Butz. *pyVPRM*: A next-generation vegetation photosynthesis and respiration model for the post-modis era. *EGUsphere*, 2025:1–45, 2025. doi: 10.5194/egusphere-2024-3692. URL https://egusphere.copernicus.org/preprints/2025/egusphere-2024-3692/.

C. Granier, S. Darras, H. Denier van der Gon, J. Doubalova, N. Elguindi, B. Galle, M. Gauss, M. Guevara, J.-P. Jalkanen, J. Kuenen, C. Liousse, B. Quack, D. Simpson, and K. Sindelarova. The copernicus atmosphere monitoring service global and regional emissions. *Copernicus Atmosphere Monitoring Service (CAMS) report*, 04 2019. doi: 10.24380/d0bn-kx16. URL https://atmosphere.copernicus.eu/sites/default/files/publications/CAMS261_2021SC1_D6.1.2-2022_202306_Docu_v1_APPROVED_Ver1.pdf.

Christine Groot Zwaaftink, Olafur Arnalds, Pavla Waldhauserova, Sabine Eckhardt, Joseph Prospero, and Andreas Stohl. Temporal and spatial variability of icelandic dust emissions and atmospheric transport. *Atmospheric Chemistry and Physics*, 17: 10865–10878, 09 2017. doi: 10.5194/acp-17-10865-2017.

Christine Groot Zwaaftink, Stephan Henne, Rona Thompson, Edward Dlugokencky, Toshinobu Machida, Jean-Daniel Paris, Motoki Sasakawa, A.J. Segers, Colm Sweeney, and Andreas Stohl. Three-dimensional methane distribution simulated with flexpart 8-ctm-1.1 constrained with observation data. *Geoscientific Model Development*, 11: 4469–4487, 11 2018. doi: 10.5194/gmd-11-4469-2018.

M. Grubb, C. Okereke, J. Arima, V. Bosetti, Y. Chen, J. Edmonds, S. Gupta, A. Köberle, S. Kverndokka, A. Malik, and L. Sulistiawati. Introduction and framing. In R. Slade A. Al Khourdajie R. van Diemen D. McCollum M. Pathak S. Some P. Vyas R. Fradera M. Belkacemi A. Hasija G. Lisboa S. Luz J. Malley P.R. Shukla, J. Skea, editor, *Climate Change 2022 - Mitigation of Climate Change: Working Group III Contribution to the Sixth Assessment Report of the Intergovernmental Panel on Climate Change*, page 151–214. Cambridge University Press, 2023. doi: 10.1017/9781009157926.003.

M. Guevara, C. Tena, M. Porquet, O. Jorba, and C. Pérez García-Pando. Hermesv3, a stand-alone multi-scale atmospheric emission modelling framework – part 1: global and regional module. *Geoscientific Model Development*, 12(5):1885–1907, 2019. doi: 10.5194/gmd-12-1885-2019. URL https://gmd.copernicus.org/articles/12/1885/2019/.

Hans Hersbach, Bill Bell, Paul Berrisford, Shoji Hirahara, András Horányi, Joaquín Muñoz Sabater, Julien Nicolas, Carole Peubey, Raluca Radu, Dinand Schepers, Adrian Simmons, Cornel Soci, Saleh Abdalla, Xavier Abellan, Gianpaolo Balsamo, Peter Bechtold, Gionata Biavati, Jean Bidlot, Massimo Bonavita, and J.-N Thépaut. The era5 global reanalysis. *Quarterly Journal of the Royal Meteorological Society*, 146, 06 2020. doi: 10.1002/qj.3803.

Pedro Jimenez and Jimy Dudhia. Improving the representation of resolved and unresolved topographic effects on surface wind in the wrf model. *Journal of Applied Meteorology and Climatology*, 51, 02 2012. doi: 10.1175/JAMC-D-11-084.1.

J. W. Kaiser, A. Heil, M. O. Andreae, A. Benedetti, N. Chubarova, L. Jones, J.-J. Morcrette, M. Razinger, M. G. Schultz, M. Suttie, and G. R. van der Werf. Biomass burning emissions estimated with a global fire assimilation system based on observed fire radiative power. *Biogeosciences*, 9(1):527–554, 2012. doi: 10.5194/bg-9-527-2012. URL `https://bg.copernicus.org/articles/9/527/2012/`.

Ahmed Kenawy, Talal Al-Awadhi, Meshal Abdullah, Rana Jawarneh, and Ammar Abulibdeh. A preliminary assessment of global co2: Spatial patterns, temporal trends, and policy implications. *Global Challenges*, page 2300184, 11 2023. doi: 10.1002/gch2.202300184.

Stefanie Kirschke, Philippe Bousquet, Philippe Ciais, M. Saunois, Josep Canadell, Edward Dlugokencky, Peter Bergamaschi, Daniel Bergmann, Donald Blake, L. Bruhwiler, Philip Cameron-Smith, Simona Castaldi, Frederic Chevallier, Liang Feng, Annemarie Fraser, Martin Heimann, E. Hodson, Sander Houweling, B. Josse, and Guang Zeng. Three decades of global methane sources and sinks. *Nature Geoscience*, 6:813–823, 10 2013. doi: 10.1038/ngeo1955.

Corinne Le Quéré, Michael Raupach, Josep Canadell, Gregg Marland, Laurent Bopp, Philippe Ciais, Scott Doney, Richard Feely, Pru Foster, Pierre Friedlingstein, Kevin Gurney, Richard Houghton, Joanna House, Chris Huntingford, Peter Levy, Mark Lomas, Joseph Majkut, Nicolas Metzl, and Ian Woodward. Trends in the sources and sinks of carbon dioxide. *Nature Geoscience*, 2:831–836, 11 2009. doi: 10.1038/ngeo689.

B. Legg and Michael Raupach. Markov-chain simulation of particle dispersion in inhomogeneous flows: The mean drift velocity induced by a gradient in eulerian velocity variance. *Boundary-Layer Meteorology*, 24:3–13, 01 1982. doi: 10.1007/BF00121796.

Jos Lelieveld, Paul J. Crutzen, and Frank J. Dentener. Changing concentration, lifetime and climate forcing of atmospheric methane. *Tellus B*, 50(2):128–150, 1998. doi: https://doi.org/10.1034/j.1600-0889.1998.t01-1-00002.x. URL `https://onlinelibrary.wiley.com/doi/abs/10.1034/j.1600-0889.1998.t01-1-00002.x`.

Bradley Matthews and Helmut Schume. Tall tower eddy covariance measurements of co2 fluxes in vienna, austria. *Atmospheric Environment*, 274:118941, 2022. ISSN 1352-2310. doi: https://doi.org/10.1016/j.atmosenv.2022.118941. URL `https://www.sciencedirect.com/science/article/pii/S1352231022000061`.

Adrien Moiret-Guigand, Gabriel Jaffrain, Alexandre Pennec, and Hans Dufourmont. Clc2018 / clcc1218 validation report. 02 2021.

E. Moxnes, Nina Kristiansen, Andreas Stohl, Lieven Clarisse, A. Durant, K. Weber, and Andreas Vogel. Separation of ash and sulfur dioxide during the 2011 grímsvötn eruption. *Journal of Geophysical Research: Atmospheres*, 119, 06 2014. doi: 10.1002/2013JD021129.

NCAR. `https://www.mmm.ucar.edu/models/wrf`.

T. Nordam, R. Kristiansen, R. Nepstad, E. van Sebille, and A. M. Booth. A comparison of eulerian and lagrangian methods for vertical particle transport in the water column. *Geoscientific Model Development*, 16(18):5339–5363, 2023. doi: 10.5194/gmd-16-5339-2023. URL `https://gmd.copernicus.org/articles/16/5339/2023/`.

Ignacio Pisso, Espen Sollum, Henrik Grythe, Nina Kristiansen, Massimo Cassiani, Sabine Eckhardt, Delia Arnold Arias, Don Morton, Rona Thompson, Christine Groot Zwaaftink, Nikolaos Evangeliou, Harald Sodemann, L. Haimberger, Stephan Henne, Dominik Brunner, John Burkhart, Anne Fouilloux, J. Brioude, Anne Tipka, and Andreas Stohl. The lagrangian particle dispersion model flexpart version 10.4. *Geoscientific Model Development*, 12:4955–4997, 12 2019. doi: 10.5194/gmd-12-4955-2019.

Shiv Priyam Raghuraman, David Paynter, V. Ramaswamy, Raymond Menzel, and Xianglei Huang. Greenhouse gas forcing and climate feedback signatures identified in hyperspectral infrared satellite observations. *Geophysical Research Letters*, 50, 12 2023. doi: 10.1029/2023GL103947.

J.T. RANDERSON, G.R. VAN DER WERF, L. GIGLIO, G.J. COLLATZ, and P.S. KASIBHATLA. Global fire emissions database, version 4.1 (gfedv4), 2017. URL `https://daac.ornl.gov/cgi-bin/dsviewer.pl?ds_id=1293`.

Andy Ridgwell, Stewart Marshall, and Keith Gregson. Consumption of atmospheric methane by soils: A process-based model. *Global Biogeochemical Cycles - GLOBAL BIOGEOCHEM CYCLE*, 13:59–70, 03 1999. doi: 10.1029/1998GB900004.

C. Rödenbeck, T. DeVries, J. Hauck, C. Le Quéré, and R. F. Keeling. Data-based estimates of interannual sea–air co_2 flux variations 1957–2020 and their relation to environmental drivers. *Biogeosciences*, 19(10):2627–2652, 2022. doi: 10.5194/bg-19-2627-2022. URL `https://bg.copernicus.org/articles/19/2627/2022/`.

Laura Rontu. Studies on orographic effects in a numerical weather prediction model. 09 2013.

Drew Shindell, Pankaj Sadavarte, I. Aben, Tomas de Oliveira Bredariol, Gabrielle Dreyfus, Lena Höglund-Isaksson, Benjamin Poulter, M. Saunois, Gavin Schmidt, Sophie Szopa, Kendra Rentz, Luke Parsons, Zhen Qu, Gregory Faluvegi, and Joannes Maasakkers. The methane imperative. *Frontiers in Science*, 2, 07 2024. doi: 10.3389/fsci.2024.1349770.

Sonnblick-Observatorium. `https://data.sonnblick.net/dataset/c2f44008`.

Andreas Stohl, M. Hittenberger, and Gerhard Wotawa. Validation of the lagrangian particle dispersion model flexpart against large scale tracer experiments. *Atmospheric Environment*, 32:4245–4264, 12 1998. doi: 10.1016/S1352-2310(98)00184-8.

Andreas Stohl, Forster C, Frank A, Seibert P, and Gerhard Wotawa. Technical note: The lagrangian particle dispersion model flexpart version 6.2. atmos. *Atmospheric Chemistry and Physics*, 5, 07 2005. doi: 10.5194/acpd-5-4739-2005.

Andreas Stohl, P. Seibert, Gerhard Wotawa, Delia Arnold Arias, John Burkhart, S. Eckhardt, Cristopher Tapia, A. Vargas, and Teppei Yasunari. Xenon-133 and caesium-137 releases into the atmosphere from the fukushima dai-ichi nuclear power plant: Determination of the source term, atmospheric dispersion, and deposition. *Atmospheric Chemistry and Physics*, 12:2313–2343, 03 2012. doi: 10.5194/acp-12-2313-2012.

Karl Taylor. Summarizing multiple aspects of model performance in a single diagram. *Journal of Geophysical Research*, 106:7183–7192, 04 2001. doi: 10.1029/2000JD900719.

R. L. Thompson and A. Stohl. Flexinvert: an atmospheric bayesian inversion framework for determining surface fluxes of trace species using an optimized grid. *Geoscientific Model Development*, 7(5):2223–2242, 2014. doi: 10.5194/gmd-7-2223-2014. URL https://gmd.copernicus.org/articles/7/2223/2014/.

D. J. Thomson. Criteria for the selection of stochastic models of particle trajectories in turbulent flows. *Journal of Fluid Mechanics*, 180:529–556, 1987. doi: 10.1017/S0022112087001940.

UWyoming. https://weather.uwyo.edu/upperair/sounding.shtml.

Marieke van der Maaten-Theunissen, Verena Quadt, and Georg Frank. *Integration of Nature Protection in Forest Policy in Austria.* 06 2013.

Martin Vojta, Andreas Plach, Rona Thompson, and Andreas Stohl. A comprehensive evaluation of the use of lagrangian particle dispersion models for inverse modeling of greenhouse gas emissions. *Geoscientific Model Development*, 15:8295–8323, 11 2022. doi: 10.5194/gmd-15-8295-2022.

Thomas Weber, Nicola A. Wiseman, and Annette Kock. Global ocean methane emissions dominated by shallow coastal waters. *Nature Communications*, 10(1):4584, Oct 2019. ISSN 2041-1723. doi: 10.1038/s41467-019-12541-7. URL https://doi.org/10.1038/s41467-019-12541-7.

Zhendong Wu, Michael Michurow, and Paul Miller. Global hourly nep, npp, gpp and heterotrophic respiration for 2010-2023 based on lpj-guess (generated in 2024), 2024. URL https://meta.icos-cp.eu/collections/E8EEk4983j5zltui3qw7HQQX.

Zhiming Xu, Zhimin Han, and Hongwei Qu. Comparison between lagrangian and eulerian approaches for prediction of particle deposition in turbulent flows. *Powder Technology*, 360:141–150, 2020. ISSN 0032-5910. doi: https://doi.org/10.1016/j.powtec.2019.09.084. URL https://www.sciencedirect.com/science/article/pii/S0032591019308204.

Lingfeng Zhang, Tongwen Li, Jingan Wu, and Hongji Yang. Global estimates of gap-free and fine-scale co2 concentrations during 2014–2020 from satellite and reanalysis data. *Environment International*, 178:108057, 06 2023. doi: 10.1016/j.envint.2023.108057.

A. Appendix

A.1. Vertical Wind Speed Analysis, Vienna

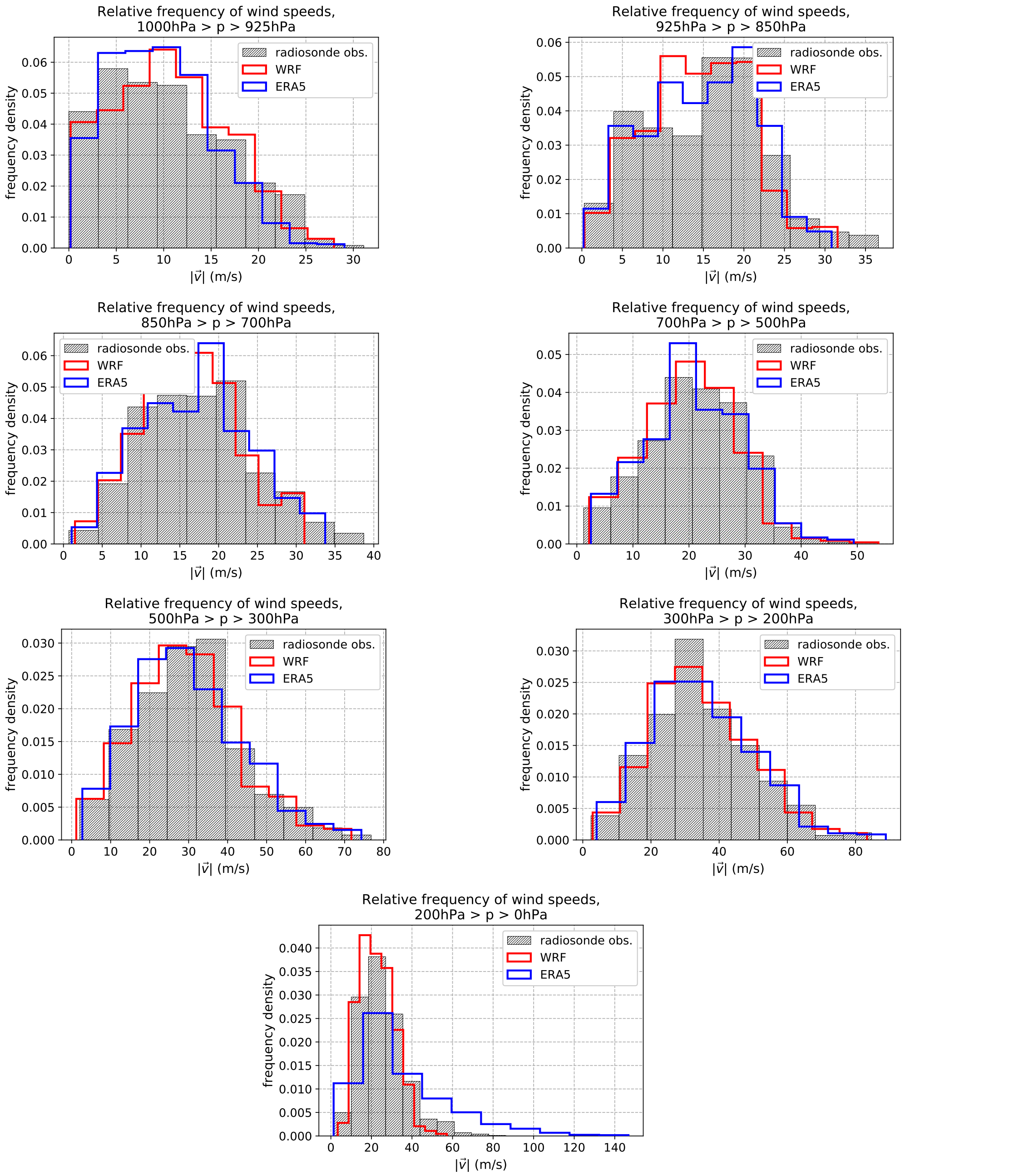

Figure A.1.: Wind speed frequencies between main pressure levels in Vienna over the test period; WRF, ERA5, and radiosonde observations.

A.2. Anthropogenic CO_2 Emissions, Vienna

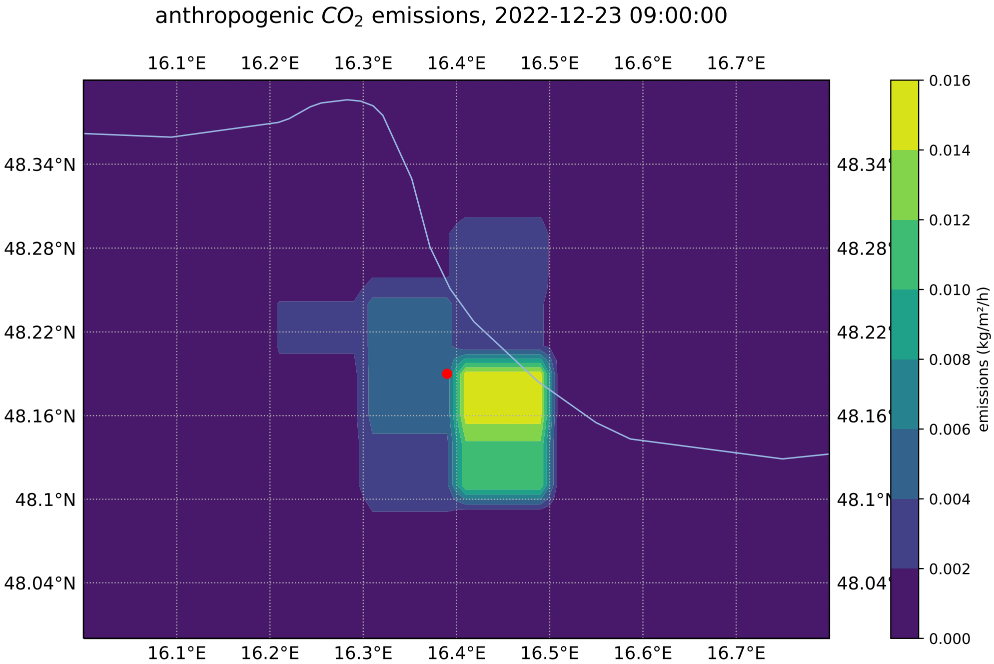

Figure A.2.: Geometry of the anthropogenic CO_2 emission inventory in the vicinity of Vienna. The time step chosen corresponds to one of the extreme values of the FLEXPART-WRF-modelled CO_2 time series; though the pattern - the Arsenal tower (red dot) being located at the boundary between a high and low emission gridcell - remains the same throughout the entire dataset.